Self-consistent kinetic calculations of helium rf glow discharges

T. J. Sommerer*
Department of Physics, University of Wisconsin, Madison, Wisconsin 53706

W. N. G. Hitchon and R. E. P. Harvey
Department of Electrical and Computer Engineering, University of Wisconsin, Madison, Wisconsin 53706

J. E. Lawler
Department of Physics, University of Wisconsin, Madison, Wisconsin 53706
(Received 27 April 1990; revised manuscript received 16 November 1990)

A theoretical study of low-pressure helium rf glow-discharge plasmas is presented. The numerical scheme provides a fully kinetic description of the electrons and singly charged He ions in one spatial dimension and predicts the electric fields present in a mutually consistent fashion. The results have implications for a variety of discharge geometries and gases. Realistic, detailed cross sections for He are used. Both the numerical algorithm and physical processes are discussed. Unlike previous theoretical studies, we find a low average electron energy (<1 eV) in the central bulk region and a weak bulk field (≈ 2 V/cm peak amplitude) that is out of phase with the strong sheath fields. The discussion emphasizes quantities that can be readily measured in order to facilitate comparison with experiment. Metastable-atom production rates are used as source terms in a diffusion-reaction model to predict metastable-atom densities. Multistep ionization due to metastable-atom–metastable-atom collisions is shown to be important for some of the conditions studied. The pressure dependence of the ion distribution at the electrode is studied. Some common approximations used in modeling discharges are examined for both suitability and possible improvement.

I. INTRODUCTION

Discharge plasmas have long been a subject of both academic and practical interest. Discharges are used in pulsed-power devices, gas lasers, semiconductor etching, thin-film deposition, and plasma modification of materials. Much interest stems from the nonequilibrium conditions routinely obtained in operating discharges. Electron "temperatures" of tens of thousands of degrees are present in an otherwise room-temperature discharge reactor and drive many useful high-temperature chemical processes. Various regions of many discharges also lack "hydrodynamic" equilibrium, meaning that the charged-particle behavior cannot be determined merely from the local electric field, but rather retains a memory of fields at other spatial locations and times. Understanding of nonhydrodynamic regions is incomplete and they are therefore a subject of academic research.

A thorough theoretical description of discharges requires that each charged species be described at the kinetic level by solution of Boltzmann's equation

$$\frac{\partial f}{\partial t}+\mathbf{v}\cdot\nabla_{\mathbf{r}} f+\mathbf{a}\cdot\nabla_{\mathbf{v}} f=Cf \tag{1}$$

(or some equivalent procedure). Here f is the phase-space distribution function, $\mathbf{r}$ and $\mathbf{v}$ are the spatial location and velocity of particles, and $\mathbf{a}$ is the acceleration due to the fields at $\mathbf{r}$. The $\nabla_{\mathbf{v}}$ operator acts in velocity space. A separate distribution function f (with an appropriate subscript) exists for each charged species. The collision operator C will in general link together different species and velocities, making the problem nonlocal in velocity space. Poisson's equation (or its dynamic generalization) then couples together all the charged species:

$$\nabla\cdot\mathbf{E}=\frac{\rho}{\epsilon_0}\ , \tag{2}$$

where $\mathbf{E}$ is the electric field, ρ the net charge density, and ϵ_0 the permittivity of free space. A direct solution of these equations avoids many of the *ad-hoc* assumptions necessary when either the particle kinetics are simplified (e.g., by using fluid equations) or when the fields are decoupled from the calculation. Neutral-particle transport is important in many discharges; it can be added in a straightforward manner to the charged-particle model, as can gas-phase chemical and wall processes through the use of tabulated reaction-rate data. Modeling a realistic discharge plasma is a formidable task because of the difficulty of describing the charged-particle behavior consistently with the fields present, because of the wide range of time scales present, and because of limited basic cross-section and reaction-rate data.

It is now possible to realistically model glow discharges at the kinetic level consistently with the fields present.[1,2] Such detailed calculations are important because the results have implications for rf discharges in many gases. To keep computational time within reason, however, only gases with simple chemistry and rudimentary wall processes are considered here. Inclusion of additional chemical and wall processes is straightforward in principle, but the time scales of some processes are extremely long; the electron plasma frequency and collision rate (which usu-

ally limit the time step of integration) may be in the range of GHz, while important chemical and wall reactions may proceed at kHz or Hz rates.

This paper presents a model of low-pressure, one-dimensional parallel-plate helium rf discharge plasmas. The electrons and singly charged helium ions are tracked at the kinetic level, and the charged-particle distributions are mutually consistent with the electric field $E(z)$, where z is the distance normal to the plates and is the one spatial dimension considered. Realistic, detailed cross sections are used for electron collisions with ground-state helium, and for charge-exchange collisions between ions and atoms. The basic numerical method has been described previously,[1,3] but has been modified for use in these rf calculations; the details of the modifications will be presented in the Appendixes. It should be emphasized that the numerical method is quite general and applicable to both rf and dc discharge calculations, as well as a wide range of nondischarge transport problems.

The results of these detailed calculations indicate a complex interaction of the high- and low-field regions and a much lower bulk average electron energy than found in other models. The present results are in good agreement with the relatively sparse experimental data. The detailed information available from a kinetic calculation allows us to study the behavior of electrons released from the electrodes by ion impact, the metastable-atom densities, and the common approximations used in discharge modeling. Before discussing the model and its results, however, we will present an overview of other discharge models and examine some relevant experimental measurements.

II. MODERN DISCHARGE THEORY

Many models of discharge plasmas are currently in use, ranging in complexity from electric circuit models to fully self-consistent kinetic calculations. This section will review the various types of models used for discharge work.

Bletzinger and Flemming[4] found that circuit models could fit the impedance characteristics of discharges in a range of pressures and rf frequencies, but that it was not obvious what capacitance or resistance to associate with more unusual processes such as the heating of electrons by rf sheath expansion. Bletzinger[5] recently obtained circuit equivalents for discharges in attaching gases and for various electrode materials. Köhler *et al.*[6] utilized a circuit model to extract the plasma potential from an experimentally measured energy distribution of ions incident on the grounded electrode in an rf argon discharge.

In this paper, "regional" models are those that use familiar approximations to describe each distinct physical region of a discharge. The resulting model may or may not be analytically solvable. A typical regional model might describe ion motion in the high-density, low-field bulk region using an ambipolar diffusion model and use the ion mobility to model ion transport in high-field collisional sheaths.

Godyak and co-workers[7–11] have developed a regional model of an entire symmetric rf discharge and compared its predictions with various He-discharge experiments. Keller and Pennebaker[12] have used a regional model to predict and analyze the characteristics of dc and rf sputtering systems. Pennebaker[13] constructed a model suitable for predicting rf discharge impedance. Lieberman[14,15] has developed models of rf sheaths under assumptions such as time-independent ion motion (collisional or collisionless) and inertialess electrons. Misium, Lichtenberg, and Lieberman have built on this latter work and developed a microscopic electrode-to-electrode discharge model.[16]

Regional models retain much of the computational simplicity of circuit methods, but their accuracy is still limited by the approximations and assumptions in the models. Some typical regional approximations will be examined in light of the results to be presented in this paper in Sec. VI to evaluate their validity and highlight possible improvements.

Continuum or fluid models have been used by Graves and Jensen,[17] Bayle, Vacquie, and Bayle,[18] Barnes, Colter, and Elta,[19] and Oh, Choi, and Choi[20] A continuum model in two spatial variables has been implemented by Boeuf.[21]

The difficulty in these models is that the system of equations is open (because the only a few moments of the electron distribution function f_e are known) and must be closed with *ad-hoc* assumptions. For instance, the primary ionization rate per unit volume S actually depends upon the ionization cross section σ_{ion} and the electron distribution function f_e:

$$S = N \int \sigma_{\text{ion}} v f_e d^3 v \tag{3}$$

but must be obtained based on the calculated quantities (neutral-particle density N, electron density, momentum, energy, or electric field). There is no proper way to extract S from this restricted subset of information.

One possible assumption is that hydrodynamic equilibrium holds; that is, that the ionization rate (for example) depends only upon the local ratio of the electric field to the neutral-particle density E/N.[19,21,22] Tables of appropriate rates have been compiled.[23] However, if the field varies rapidly in space or time, particles will retain a "memory" of fields at earlier times and locations and the hydrodynamic approximation is no longer valid.[24]

One might instead assume that the average energy found from the fluid equations corresponds to the temperature of a Maxwellian distribution function;[17] the various rates could then be found using this assumed distribution. We refer to models in which the distribution function is assumed as based on the moment method.

The moment method has been thoroughly scrutinized by Ingold[25,26] for its applicability to dc discharges and swarm (spatially invariant field) experiments. Electron excitation and ionization at very high E/N have been analyzed using a beam model.[27]

Because of the numerical difficulty of a direct solution of the full Boltzmann equation, attempts to use it have usually been limited to calculations in which spatial variations are ignored or where the field configuration is imposed.

Kitamori, Tagashira, and Sakai[28] have used finite

differences to solve Boltzmann's equation in three velocity variables and study relaxation processes in neon. Lucas and Saelee[29] have compared results using both Monte Carlo and Boltzmann techniques. Tagashira, Sakai, and Sakamoto[30] have analyzed avalanches in argon using Boltzmann's equation and compared the results to Monte Carlo simulations.[31]

Finite-difference methods are in general computationally too intensive for use in more complex discharge problems. The time step is strictly limited so that *at no location on the mesh* do particles cross more than one cell per time step (the Courant criterion[32]). This global limit on the time step applies in all independent variables (particles cannot move more than one spatial cell per time step, nor be accelerated more than one velocity cell). Finite-difference formulations can also suffer from excessive numerical diffusion—the nonphysical movement of particles about the mesh. "Flux-corrected" algorithms partially alleviate this second drawback.[33–38]

Segur and Keller[39] have manipulated Boltzmann's equation into a purely integral form and solved both swarm and cathode-fall problems with imposed electric fields, obtaining good agreement with the Monte Carlo (MC) predictions of Boeuf and Marode.[24,40]

Boltzmann's equation can also be expanded using a polynomial series to yield a set of simpler but coupled differential equations. The angular part of the velocity-space distribution is expanded in spherical harmonics (Legendre polynomials for cylindrically symmetric problems). Two-term and "n-term"[41–44] solutions have proven extremely useful for problems where the distribution function is nearly isotropic.

Tran Ngoc An, Marode, and Johnson[45] have used a MC simulation in two variables (distance from the cathode and velocity along the discharge axis) to calculate the properties of a dc helium cathode fall. A related two-variable model has been used to examine electron behavior in the cathode fall of helium[46] and argon[47] discharges. Boeuf and Marode[40] analyzed He dc discharges using the null collision technique in a model in three independent variables which allowed for electron motion and scattering transverse to the discharge axis. MC simulations using fixed electric fields have been used to study the cathode fall of a helium discharge,[48] a helium hollow-cathode discharge,[49] and electron avalanches in argon.[31] Moratz, Pitchford, and Bardsley[50] used MC methods to study the suitability of the hydrodynamic approximation in spatially varying fields in nitrogen.

Den Hartog, Doughty, and Lawler[51] used the Boeuf and Marode algorithm[40] and imposed the fields as measured using noninvasive optogalvanic techniques. The MC predictions for metastable production and cathode-current balance in a dc discharge were in good agreement with their experimental measurements.

Kushner[52,53] has used MC simulations to model rf discharges and study the electron energy distribution in various molecular gases, including Ar-SiH_4 mixtures. Electrons were run in an imposed rf field until memory of their initial state had vanished. A degree of consistency with the fields was achieved by adjusting the bulk electric field amplitude to balance ion production and loss.

Particle-in-cell (PIC) models[54,55] were first applied to discharge plasmas by Boswell and Morey.[56] The PIC method is hampered by the need to deal with the high number densities and large density gradients (in sheaths) present in typical glow discharges. Accurate solution of Poisson's equation may require very large numbers of particles to give credible statistics, especially in regions were the plasma is very close to neutral. Methods to reduce the effects of statistical noise (e.g., Fourier analyzing the field[54,55]) are not suited for glow discharges because large field and density gradients exist.

Surendra, Graves, and Morey[57] have studied a 30-MHz discharge in a heliumlike gas, and report the observation of an "ionization pulse" originating at the sheath-bulk boundary and traversing the bulk. They also find the bulk electrons to be quite energetic [average energies of several to 10 eV (Ref. 58)] in comparison to the results to be presented here (<1 eV). Date, Kitamori, and Tagashira[59] have used the PIC method to simulate both atomic and simple molecular gas discharges, while Vender and Boswell[60] have used PIC models in model gases to evaluate simple analytic discharge models. PIC calculations are perhaps the closest relative of the "convective-scheme" (CS) method to be presented here.

The diversity of conditions in rf discharges has led to the development of models that selectively combine elements of several of the models just described. Where regional models separate the discharge into spatial regions, a hybrid model groups electrons based on their physical behavior.

Hybrid models have been used to examine the role of secondary electrons in rf discharges. Particle simulations and the beam models are suited for modeling the directed, energetic motion of secondary electrons, but not for describing randomized, low-energy electron motion at high plasma density. A continuum model can be grafted to the energetic electron model to describe this latter group of electrons.

Boeuf and Belenguer[61,62] have applied a hybrid model to rf discharges and found that in higher-pressure discharges also having secondary electrons, dramatic increases in the plasma density can be obtained once the applied voltage (for example) is increased beyond some critical value. In their work a monoenergetic beam is used to describe the secondary electrons released from the electrode, and a "pure" continuum model describes the remainder of the electrons. This model has also been used to investigate photoelectron-initiated avalanches in dc discharges.[63]

Surendra, Graves, and Jellum[64] have constructed a hybrid model to study atomic dc glow discharges. Schoenbach, Chen, and Schaefer[65] have studied an abnormal glow discharge in a He-SF_6 mixture. Both used PIC-continuum hybrids; the PIC method describes fast electrons in much greater detail than a beam model, and allows for other important processes such as angular electron scattering.

III. EXPERIMENTAL WORK ON rf DISCHARGES

Some relevant experimental work will be reviewed in this section. By no means is this an overview of rf

discharge work; only notable results from rf and selected dc discharges in simple gases and well-defined geometries will be covered here.

The distribution of ions at the cathode of a dc discharge has been measured by Davis and Vanderslice,[66] while Coburn and Kay[67] have studied the relationship between ion bombardment and electrical characteristics. The electrical characteristics of rf discharges in argon have been examined by Bletzinger and Flemming,[4] and compared with a circuit model. Bletzinger[5] has investigated the effects of the addition of attaching gases to an argon discharge, finding dramatically thinner sheaths and much stronger sheath fields.

A detailed survey of an argon rf discharge has been made by Godyak and Piejak,[68–71] primarily through use of Langmuir probes. Earlier work in hydrogen and argon by Levitskii,[72] and in helium[8–10,73] demonstrated the existence of several discharge operating regimes, the regime being related to the importance of secondary-electron emission. Specifically, dramatic increases in bulk density were observed as the operating voltage was increased beyond a certain threshold. Below the threshold the discharge operates in the so-called α regime, where the bulk electrons are sufficiently energetic to provide the ionization necessary to sustain the discharge. The regime above the threshold is referred to as the γ regime; avalanching secondary electrons sustain the discharge, and a high bulk temperature is not required. A hybrid model[61,62] indicates that the transition voltage is dependent upon the secondary-electron emission coefficient and hence the electrode material. We will consider the α and γ regimes in Sec. VI and show that neither the γ mechanism nor the α mechanism (as originally defined with a high average energy for bulk electrons) can be considered the dominant sustaining mechanism for the discharges of interest here.

Gottscho and co-workers have studied rf and dc discharges, usually in gases useful for semiconductor device fabrication.[74–76] Spatial and temporal maps of the electric field were obtained using noninvasive laser techniques for discharges in BCl_3, Cl_2, and BCl_3-Ar mixtures at rf frequencies up to 10 MHz. The electronegativity of the gas and the ability of ions to respond to the time-varying fields at these lower rf frequencies are responsible for interesting sheath dynamics and double-layer formation. Various electronegative gases have been modeled using continuum[22] and hybrid models[61] and the results are in general qualitative agreement with this experimental work.

Hebner *et al.*[77,78] have studied rf discharges in various gases using a framing camera, microwave interferometry, and microwave radiometry, and have found an extremely low bulk electron temperature of only 500 K in helium. This astonishingly low energy might be disbelieved were it not for the unambiguous temperature and density results possible through the microwave techniques employed. Under similar conditions, by contrast, the continuum model of Graves and Jensen[17] predicts a bulk electron energy of several eV for a heliumlike gas while Boeuf and Belenguer[61] assume a value of 1 eV in a hybrid model of a helium discharge.

The very low bulk electron energies led Hebner *et al.*[77,78] to observe that the bulk region of an rf discharge can be much like the negative glow of a dc discharge. Experimental work by Doughty *et al.*[79–81] and Den Hartog *et al.*[51,82] using noninvasive laser techniques found a high density of rather low-energy (0.1–0.25 eV) electrons in the negative glow of their dc He discharge. Earlier work in somewhat similar dc discharges by Anderson[83,84] reported even lower average energies using probe and microwave techniques. Ionization and excitation in the negative glow are sustained by a low density of high-energy "beam" electrons injected from the cathode fall. An rf discharge, at least in an electropositive gas, can be quite similar; the low-energy bulk electrons move gently back and forth during an rf cycle. Excitation and ionization are driven by a low density of high-energy electrons that are accelerated in the instantaneous cathode sheath of the rf discharge.

The perceived need for an in-depth, systematic, experimental study of a "simple" rf discharge has led to the proposal of a standard, well-characterized rf research reactor. The so-called "rf reference cell" is currently being developed for a parallel-plate discharge in argon.[85]

IV. PHYSICAL CONSIDERATIONS

In this work we consider a hypothetical parallel-plate discharge reactor shown in Fig. 1.

(1) The discharge consists of equal-area electrodes and of vacuum containment walls, the latter being sufficiently far from the active discharge region to be ignored. The size of the discharge plates is assumed much larger than their separation d such that fringing effects can be ignored. These assumptions lead to the use of an infinite-plane-parallel geometry where only one spatial variable is required (the location on the z axis perpendicular to the electrodes). Quantitative comparison of the results presented here with experimental measurements requires that the experiment closely approximate a symmetric plane-parallel discharge. Arguments based on diffusion lengths suggest that the plate radius must be at least three times the plate separation.

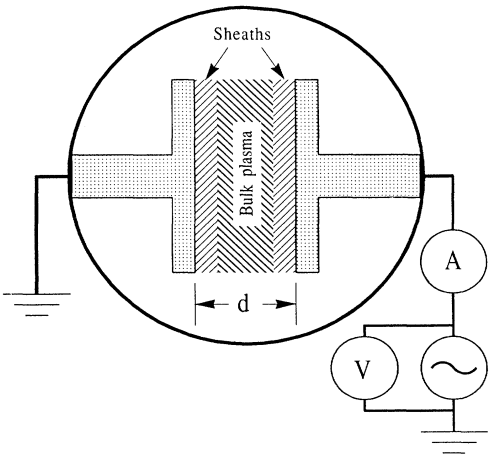

FIG. 1. A schematic of the discharge configuration modeled.

(2) The voltage source is ideal, generating a pure sine wave of amplitude V^0.

(3) The gas is weakly ionized, with the plasma density less than $\approx 10^{-5}$ of the neutral-particle density; collisions between charged particles and neutral particles dominate, although collisions between charged particles can be significant (Sec. VI).

(4) Electrons scatter isotropically from both elastic and inelastic collisions with neutral particles, with the highly anisotropic elastic cross section replaced by the isotropic momentum transfer cross section. An electron energy loss of $2(m/M)(\frac{1}{2}mv^2-\frac{3}{2}kT_g)$ during each elastic collision is included, where $\frac{1}{2}mv^2$ is the initial electron kinetic energy of the electron, $\frac{3}{2}kT_g$ is the mean kinetic energy of the neutral-particle gas, and m and M are the mass of the electron and neutral particle, respectively.

(5) Only singly charged ions exist, with charge-exchange collisions dominating their motion. After scattering, ions have a Maxwellian distribution at the neutral-particle temperature. This approximation is quite accurate at high E/N,[86,87] but less so at low E/N because elastic ion–neutral-species collisions are neglected. Its primary advantage is that the CS ion calculation requires only one space and one velocity variable. The charge-exchange cross section at low energies is adjusted to reproduce measured ion mobilities and thus compensate for the neglect of elastic scattering at low E/N.

(6) Thermal motion of the neutral particles is included in a simple fashion when finding electron–neutral-particle collision rates. The relative speed of the electron and neutral particle is taken to be $\sqrt{v^2+8kT_g/(\pi M)}$, where v is the electron speed (from the CS mesh) and $\sqrt{8kT_g/(\pi M)}$ is the usual expression for average speed for a Maxwellian distribution of neutral particles. This simple method reproduces the correct behavior in both limits where $v^2 \gg 8kT_g/(\pi M)$ and $v^2 \ll 8kT_g/(\pi M)$.

(7) Both the thermal motion of the neutral particles and the assumed Maxwellian distribution of ion speeds transverse to the discharge axis are included in an analogous manner. The relative collision speed is taken to be $\sqrt{v_z^2+8kT_g/(\pi M/2)}$, where v_z is the ion velocity along the discharge axis (from the CS mesh). We have explicitly displayed the use of the reduced ion–neutral-particle mass $M/2$.

Aside from the inclusion of electron energy loss during elastic electron–neutral-particle collisions, electron–neutral-particle collisions are handled exactly as in Ref. 1. The semi-empirical cross sections of Alkhazov[88] are used for inelastic electron–neutral-particle processes. The elastic momentum transfer cross section for electrons is calculated from the differential elastic cross section of LaBahn and Callaway.[89] The ion–neutral-particle resonant charge-exchange cross section is that extracted from mobility data by Helm.[90] Many previous models of He discharges have used an identical or very similar set of He cross sections.[1,2,24,40,45,51] In addition, Coulomb collisions between electrons are included in some runs using a method analogous to that of Weng and Kushner.[91] Multistep ionization is discussed in Sec. V C.

A proper description of the electron-scattering process requires at least two velocity coordinates (three dimensions). DiCarlo and Kushner[38] have compared results from Monte Carlo,[40,45] beam,[46] and their own finite-difference calculations[38] of electrons in a helium dc cathode fall in one- and two-velocity variables. Electron models in only one-velocity coordinate result in more forward scattering and energy transport out of the cathode fall and into the glow. The excellent agreement between a 3D Monte Carlo code[40,51] and experiment[51] is evidence that a 3D description is not only necessary, but also sufficient.

These assumptions lead to the following model for the helium discharges under study. One spatial coordinate z is sufficient for plane-parallel geometry. For the electron calculation we choose as velocity coordinates the magnitude of the velocity vector v and the angle θ between the velocity vector and the $+z$ axis. This coordinate system simplifies scattering calculations because an isotropic distribution of particles is uniformly distributed in μ, where $\mu=\cos\theta$. This choice makes calculation of ballistic electron motion less convenient since θ is ill defined at $v=0$.

The requirements on the ion model are much less stringent because the dominant ion-collision process is charge exchange. The charge-exchange collision between a fast ion and a thermal neutral particle of equal mass can be thought of as producing a fast neutral particle and a thermal ion. An ion model with two independent variables z and v_z, where v_z is the velocity along the discharge axis, is sufficient. The ion velocity distribution transverse to the discharge axis is assumed to be Maxwellian.

V. NUMERICAL METHOD

Various implementations of the "convective scheme" (CS) have been described in the literature. Earlier work using propagators was able to describe thin-film growth.[92,93] The CS has been previously used to model ions in a plasma sheath or presheath,[3,94,95] and examine plasmas in magnetic confinement devices.[96] Reference 3 contains a thorough description of one CS implementation. The authors have previously combined a kinetic CS model of the electrons in the cathode fall of a dc He discharge with a mobility description of the ions to obtain a self-consistent model of the cathode fall,[1] and have reported in a recent paper the use of a self-consistent kinetic model to describe ions and electrons in He rf discharges.[2] This section briefly summarizes that material and the improvements necessary for accurate calculations of rf glow discharges.

A. General description

Figure 1 of Ref. 1 is reproduced in enhanced form here as Fig. 2 and provides the basis for describing the improvements made to the algorithm since that time. The idea of the CS as applied to this problem is, given a suitable numerical mesh throughout phase space, to move the particles associated with the individual cells of the mesh to a new location based on their initial coordinates (position and velocity), the fields present (here assumed to be purely electric), the collision probability, and the time step. The particles are then distributed into cells of the

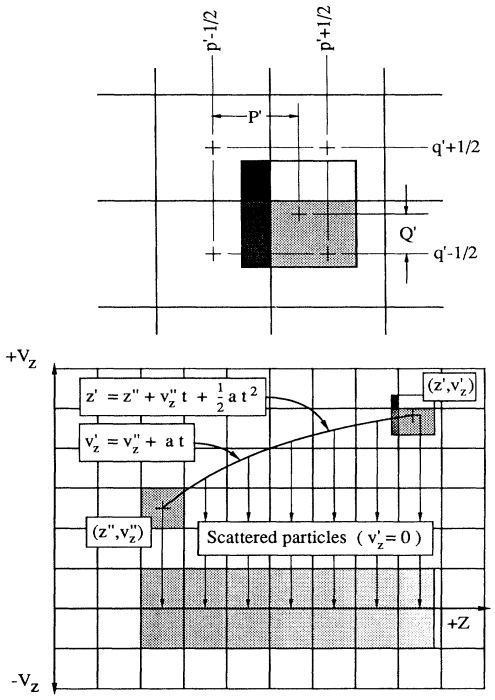

FIG. 2. An illustration of a simple convective scheme implementation in two independent variables z, the distance from the left electrode (see Fig. 1), and v_z the velocity along the z axis. The force (electric field) is assumed constant. The scattering shown in analogous to ion–neutral-particle resonant charge exchange; particles stop after collision. The mesh straddles $v_z=0$ to avoid possible singularities.

mesh based on the phase-space overlap as indicated in the upper portion of Fig. 2. In the limit of infinitely small mesh cells, the initial particle density in a single cell resembles a δ function in phase space, and hence there is a connection between the CS and Green's functions or propagators. The solution of kinetic equations by this method is straightforward because the appropriate propagator is intuitively obvious, at least for time steps much less than a mean collision time. This algorithm is described in detail in Secs. III and IV of Ref. 1 and was used there to produce a self-consistent, kinetic description of the electrons in the cathode fall of a helium glow discharge. Improvements to this basic CS were found necessary to accurately model rf discharges; the details are found in Appendix A. A method for rapidly attaining convergence has been developed and is outlined in Appendix B.

B. Method of calculation

The calculations presented here are typically started with a uniform spatial density of electrons and ions. Particles are loaded into the lowest nonzero velocity cell of the mesh with an isotropic angular distribution, at the phase of the rf cycle where there is no net potential applied across the discharge and where the left ($z=0$) sheath is expanding. The details of the initial distribution are rather unimportant for these rf calculations, but may be chosen to satisfy any desired initial condition. The CS is quite robust and can start in a most realistic fashion from nearly any initial condition.

The calculation then proceeds in the applied rf potential until convergence is reached. The "scale-up" procedure has been used to speed this portion of the calculation (Appendix B). Quantities such as the total number of particles in the discharge or the sum of their kinetic energies are compared at the same phase of successive rf cycles, and the run is declared converged when the fractional change in the quantities is less than 5×10^{-4}. For these discharges we estimate that this convergence criterion corresponds to a maximum deviation of $\pm15\%$ in the predicted discharge quantities from those of a perfectly converged solution. Uncertainties in the electron–neutral-particle cross sections have been discussed elsewhere,[1,51,88,89] but can be assigned an overall value of $\pm25\%$. The resonant ion–neutral-particle charge-exchange cross section is known to better than $\pm10\%$.

C. Multistep ionization

Absolute measurements of metastable-atom densities are possible through the use of laser-induced fluorescence and absorption spectroscopy. Metastable atoms therefore provide a valuable link between theory and experiment. The metastable production rates from the kinetic calculation are fed into a diffusion-reaction model based on propagators to obtain maps of helium metastable-atom density.

We calculate excitation to levels $n\,^1S$, $n\,^3S$, $n\,^1P$, $n\,^3P$, $n\,^1D$, $n\,^3D$, where the principal quantum number $n\le5$. The cross sections are taken from Alkhazov.[88] Excitations to all triplet levels are assumed to cascade to the metastable $2\,^3S$ level. The singlet manifold is more complex because of the optically allowed transitions from the $n\,^1P$ levels to the ground state. Transitions to the ground state are radiatively trapped. Under the present discharge conditions natural and pressure broadening of the transitions dominate the trapped decay rate. The pressure broadening is found from the work of Ali and Griem.[97] Trapped radiative decay rates are known analytically for infinite-slab geometry,[98] and vacuum decay rates[99] are used between excited levels.

Metastable-atom transport is adequately described by solving the diffusion equation for each species:

$$\frac{\partial n}{\partial t}-D\nabla^2 n=R\ , \tag{4}$$

where n, D, and R are the density, diffusion coefficient, and net source rate per unit volume for the particular species. The appropriate one-dimensional propagator[100] for a δ-function distribution initially at z_0 after a time Δt is

$$p=\frac{1}{\sqrt{4\pi D\Delta t}}\exp\left[\frac{-(z-z_0)^2}{4D\Delta t}\right]\ . \tag{5}$$

The net source rate R for each metastable species is found using the full kinetic discharge calculation in combination with reaction-rate data. Three reaction processes are included:

$$\mathrm{He}^* + \mathrm{He}^* \xrightarrow{R_{MM}} \mathrm{He} + \mathrm{He}^+ + e^- , \quad (6)$$

$$\mathrm{He}(2\,^1S) + \mathrm{He} \xrightarrow{R_{M0}} \mathrm{He} + \mathrm{He} + h\nu , \quad (7)$$

$$\mathrm{He}(2\,^1S) + e^- \xrightarrow{R_{Me}} \mathrm{He}(2\,^3S) + e^- + 0.79\ \mathrm{eV} . \quad (8)$$

He* denotes either species of metastable atoms; both may be destroyed upon collision with other metastable atoms [Eq. (6)] with a rate constant R_{MM}. Direct destruction of triplet-state atoms [He($2\,^3S$)] in binary collisions with neutral He is spin forbidden, so only the singlet-state atom–neutral-atom process is shown [Eq. (7)], with rate constant R_{M0}. Equation (8) shows the exothermic conversion of singlet metastable atoms [He($2\,^1S$)] to triplet-state atoms in collisions with low-energy electrons. The rate governing this process R_{Me} is dependent upon the electron temperature.[101] The continuity equations governing these processes are discussed in Ref. 51 and solved there for a dc discharge.

The reaction-rate data are shown in Table I. Where only cross-section data σ are available, the rate σv is found using a speed $v = \sqrt{8kT_g/(\pi M_r)}$, where T_g is the temperature (300 K for neutral particles) and M_r is the reduced mass of the colliding particles. The electron temperature is determined from the electron kinetic energy. The raw metastable-atom–metastable-atom collision rates must be doubled to account for the loss of two metastable atoms per event and obtain the R_{MM} shown in Table I.

VI. RESULTS AND DISCUSSION

Results from four rf discharge calculations have been presented in an earlier paper.[2] A set of "benchmark" discharge parameters was chosen for one discharge. One of the chosen parameters was then varied for each of three additional runs presented in the paper. In this paper we present additional results from the runs in Ref. 2 and continue to work outward in parameter space from the benchmark conditions. The discharges studied and results obtained are summarized in Table II.

TABLE I. Reaction data used in metastable transport calculation. D is the diffusion coefficient, R_{MM} the rate of metastable-atom destruction in metastable-atom–metastable-atom collisions, R_{M0} the rate of metastable-atom destruction in metastable-atom–ground-state-atom collisions, and σ_{Me} the cross section for singlet-to-triplet conversion.

$D_{2\,^1S}N$	1.4×10^{19} cm^{-1}s^{-1} [a]
$D_{2\,^3S}N$	1.51×10^{19} cm^{-1}s^{-1} [a]
R_{MM}	3.9×10^{-9} cm^{3}s^{-1} [b]
R_{M0}	5.8×10^{-15} cm^{3}s^{-1} [a]
σ_{Me}	3×10^{-14} cm^2 [c]

[a]Phelps (Ref. 102).
[b]Cross section from Phelps and Molnar (Ref. 103) with $R=\sigma v$ and $v=\sqrt{8kT_g/(\pi M_r)}$, where $T_g=300$ K and M_r is the reduced mass.
[c]Value from Phelps (Ref. 102) for electrons at 300 K. Electron-temperature dependence from Fon (Ref. 101).

TABLE II. Summary of the results from the ten He rf discharges. All discharges have an electrode spacing $d=4$ cm. Runs 1–4 were presented in a previous paper (Ref. 2).

Quantity	Units	Description	Run No. 1	2	3	4	5	6	7	8	9	10
N	10^{15} cm^{-3}	Neutral-He density	3.535	3.535	3.535	3.535	3.535	3.535	7.070	7.070	7.070	14.14
V^0	V	Applied potential amplitude	500	500	500	250	500	1000	500	500	250	250
f_0	MHz	Applied rf frequency	13.56	10	13.56	13.56	13.56	13.56	13.56	13.56	13.56	13.56
γ		Secondary-emission coefficient	0.1	0.1	0.0	0.1	0.3	0.1	0.1	0.0	0.1	0.1
j_D^0	mA cm^{-2}	Current density amplitude	2.7	1.5	2.6	1.3	3.0	5.6	4.1	3.9	1.6	2.0
$\overline{V^{dc}(d/2)}$	V	Time-averaged plasma potential	221	219	222	121	227	428	227	227	122	116
$L^{\max}$	cm	Maximum sheath length	1.1	1.4	1.1	1.1	1.1	1.1	0.8	0.9	1.0	0.8
$n_e^{\max}$	10^9 cm^{-3}	Peak plasma density	10	3.6	9.0	3.6	15	31	48	39	7.3	17
$S^{\max}$	10^{14} cm^{-3}s^{-1}	Peak ionization rate per unit volume	9.0	5.3	8.3	2.8	12	26	24	19	5.7	9.7
$\overline{S(d/2)}$	10^{14} cm^{-3}s^{-1}	Time-averaged bulk ionization rate per unit volume	5.5	3.2	5.0	1.7	7.9	16	12	8.2	2.2	1.3
$\frac{1}{2}m\langle v^2\rangle_e$	eV	Bulk electron kinetic energy at $z=d/2$, using time-averaged mean-squared velocity	0.54	0.90	0.58	0.68	0.51	0.47	0.23	0.25	0.68	0.49
$E^0(d/2)$	V/cm	Bulk field amplitude	1.9	1.9	1.8	1.8	1.8	1.8	2.0	2.2	1.4	1.3

A. The benchmark discharge

The chosen benchmark discharge conditions were a peak driving voltage $V^0=500$ V, a secondary-emission coefficient $\gamma=0.1$, an rf frequency $f_0=13.56$ MHz, and a neutral-helium density $N=3.535\times10^{15}$ cm^{-3}. We first consider the case when metastable atom–metastable-atom ionization and Coulomb collisions are neglected. In this case, these conditions represent a limiting low-pressure discharge in that the simulated discharge could not be sustained after halving N. Low-energy electrons will undergo several elastic collisions in crossing the discharge, but the mean free path for inelastic events is several times the electrode gap. Results from this calculation are shown in Fig. 3 and are representative of the results from other discharge operating points.

Figure 3(a) is a contour plot of electric field. As reported in another paper,[2] we find sheath behavior consistent with other models, but also find a weak field in the bulk region (E_{bulk}) which is distinctly out of phase with the sheath fields. We will elaborate on the implications in the next section.

The operating frequency of these discharges is between the ion and electron plasma frequencies. The ions therefore mainly are affected only by an average field, while the electrons are able to respond to the time-varying fields. The electron behavior is displayed in Fig. 3(b), which shows that high-field regions are nearly devoid of electrons, while the bulk electron density is substantially indifferent to the oscillating sheath fields. Also of interest is the degree to which electrons fill into the volume near the electrode when the field there is weak; the electrons are aided by E_{bulk}, which tends to push them in behind retreating sheaths. These electrons play an important role in the discharge because it is principally these electrons which are heated when the sheath subsequently expands.

This latter process can be seen in Fig. 3(c), which shows the power deposition into the electrons calculated from the usual expression $P=-|e|n_e\langle v_z\rangle_e E_z$. (Brackets with an appropriate subscript are used throughout this paper to represent a quantity averaged over the distribution function, thus $\langle v_z\rangle_e=\int v_z f_e d^3v/\int f_e d^3v$.) The process whereby electrons gain energy from expanding sheaths is sometimes called "wave riding,"[52] although this term may be misleading; the moving sheaths are not plasma waves. The electrons may be able to bounce off the sheath in a collisionless process and gain energy "stochastically" by making multiple bounces between the two sheaths.[7,14] At higher neutral-particle pressures, electrons may also undergo several collisions while under the influence of the strong sheath fields, in an essentially ohmic heating process. Both can occur in the same discharge, depending upon the electron energy. We refer to them collectively as "sheath heating" or heating due to sheath expansion.

Moving sheaths also removes energy from the discharge electrons. Electrons which move into the high-field sheath region while the sheath is contracting will give up energy to the field. An (imperfect) analogy can be drawn to a ball (the electron) elastically striking a massive moving wall (the sheath). If the velocity vectors

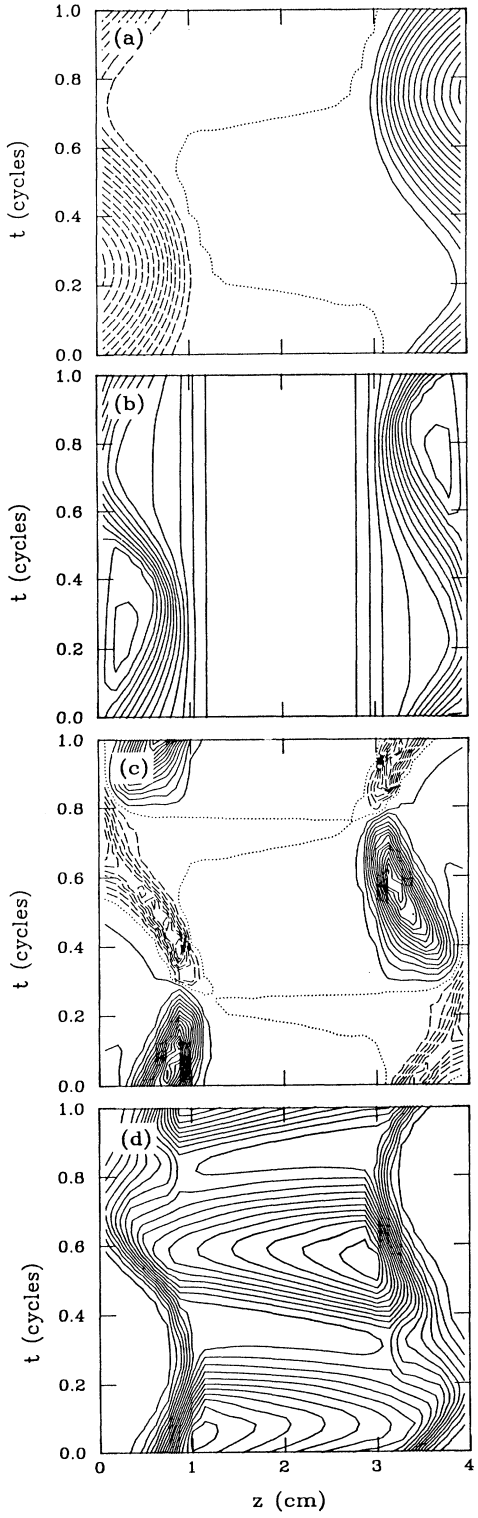

FIG. 3. Contour plots of the benchmark discharge results. In all contour plots in this paper, solid, dotted, and dashed lines denote positive, zero, and negative values, respectively. Shown over one rf cycle are (a) the electric field, (b) $\log_{10}$ of the electron relative density which peaks in the center (at 1×10^{10} cm^{-3}), (c) the power deposition into the electrons, and (d) the primary ionization rate per unit volume. The contour spacing is (a) 50 V/cm, (b) $\frac{1}{3}$, (c) 5×10^{16} eV cm^{-3} s^{-1}, and (d) 5×10^{13} cm^{-3} s^{-1}.

TABLE III. Amplitude A and phase ϕ of the first three nonzero Fourier components of the discharge current. All A_2 and A_4 vanish for a symmetric discharge (see text). Amplitudes are given as a percentage of the fundamental A_1(all $A_1=100\%$), and phases are relative to the applied voltage (a pure sine wave).

Run	ϕ_1/π	A_3	ϕ_3/π	A_5	ϕ_5/π
1	0.46	5.4	0.39	0.4	0.50
2	0.44	6.2	0.34	0.6	0.48
3	0.47	6.5	0.43	0.7	0.38
4	0.44	6.2	0.34	0.6	0.48
5	0.45	5.9	0.41	0.5	−0.39
6	0.45	7.5	0.46	1.1	−0.35
7	0.44	5.8	0.41	1.6	−0.49
8	0.45	6.2	0.38	1.2	0.36
9	0.46	3.6	0.31	0.2	0.13
10	0.46	4.4	0.32	0.3	0.40

of the wall and ball are initially antiparallel, the ball will gain energy during the collision, but lose energy if the velocity vectors are initially parallel.

Power deposited into electrons will ultimately manifest itself as electronic excitation and ionization of neutral particles. The ionization rate per unit volume is shown in Fig. 3(d), and as expected, reflects the power deposition. The mean free path for ionization is more than a discharge length, so the inelastic processes resulting from the localized power input appear throughout the discharge; the rate per unit volume drops roughly exponentially from the location where the power is deposited to the opposite sheath edge.

B. *V-I* characteristics

We now turn to specific characteristics of all the discharges.

The amplitude and phase of the first three nonzero Fourier components of the discharge current are shown in Table III. The amplitudes are a percentage of the amplitude of the current fundamental. Phases are measured relative to the phase of the applied voltage fundamental and folded back into the range $-\pi/2<\phi<\pi/2$.

The even Fourier components of the current must vanish for a symmetric discharge. An even Fourier component of the current would have the same sign (corresponding to current in the $+z$ or $-z$ direction) at two phases in the rf cycle separated by one-half of the rf cycle (differing in phase by π), a situation disallowed by symmetry.

As expected, the discharges are all dominantly capacitive, with the current leading the applied voltage by nearly $\pi/2$. The most significant variations observed are those associated with changes in the neutral-particle density. The values reported here for the fifth Fourier component (especially the phase) are comparable to their uncertainty given the quoted convergence criterion.

C. Bulk electric field

The bulk field waveform for the benchmark discharge, for run 7 (twice the neutral-particle density but otherwise identical) and for run 10 (four times the neutral-particle density and half the applied potential) are presented here in Fig. 4. The most noticeable variation occurs in the bulk field waveform, which becomes more like a pure sinewave at the higher pressures. Aside from this difference, and ignoring differences in absolute magnitude between the various runs, the waveforms for the current density j_D, the field at the $z=0$ electrode $E(0)$, and the bulk field $E(d/2)$ are remarkably similar in spite of substantial differences in the discharge operating point. Preliminary CS results in rf argon discharges indicate similar E_{bulk} behavior. Sato and Lieberman[104] have found a similar E_{bulk} using an electron beam deflection technique to measure the E_{bulk} in 2 and 23 mTorr Ar rf discharges. The electrons carry nearly all the discharge current through the bulk; this phase of E_{bulk} is required to satisfy current continuity.

A comparison of runs 4, 9, and 10 (identical except for N) indicates a trend toward generally weaker bulk fields at higher N. [We note here the $E(d/2)$ as plotted in Fig. 4 has been smoothed to remove noise at the 5% level. None of the other results presented here have been smoothed, nor have any of the time-dependent results been averaged by sampling the quantity at the same phase of successive rf cycles.]

The field reversal and the average electron motion are interrelated. The field reversal is for the most part located at the plasma edge of the contracting sheath. This region was just depleted of electrons by the sheath, which had been expanding at an earlier instant of the rf cycle. As the sheath reaches its maximum extent and begins to contract, E_{bulk} acts to draw electrons from the bulk into the electron-depleted region in front of the now-contracting sheath.

The effect of E_{bulk} has been studied by modifying the true field configuration and looking for changes in the ionization rate. This "tracking" calculation enables us to study individual portions of the electron energy distribution function. The tracking calculation starts from the converged benchmark solution. The distribution function is cleared of all electrons except those which are at one selected speed and are also in spatial locations where the field is weak ($|E|<5$ V/cm). These electrons are then

run for several cycles in the true benchmark field and ionization events are tabulated. The same experiment is then repeated with a modified field configuration. The first modification consisted of setting the field to zero any time its actual magnitude was less than 5 V/cm. This change was found to reduce ionization due to low-energy electrons but increase that due to high-energy electrons. The second modification was to invert the sign of the field (compared to the true benchmark field) in regions where its magnitude is less than 5 V/cm. This latter modification magnifies the changes observed when E_{bulk} was set to zero. The cumulative ionization for electrons initially at two different energies is shown in Fig. 5. The effects beyond the first cycle shown in Fig. 5 are less important as the distribution bears little resemblance to the initial distribution. Because we are only interested in the relative ionization rate, *the vertical scales for each electron energy are different.*

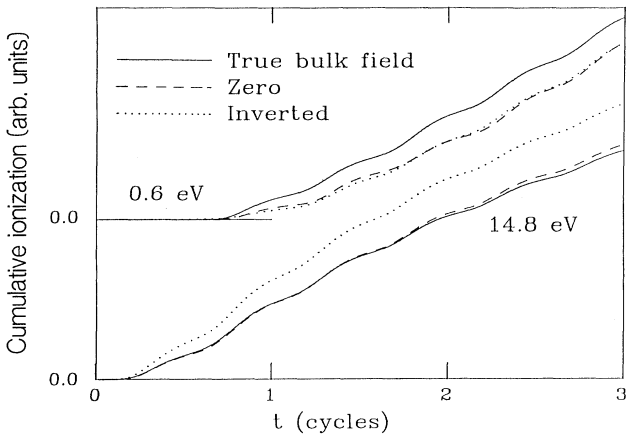

FIG. 5. Cumulative ionizations due to electrons initially having 0.6 and 14.8 eV in the low-field regions (<5 V/cm) of the benchmark discharge (solid lines). Changing the bulk field affects the ionization. Low-energy bulk electrons are not pushed toward the electrodes as the sheaths retreat after either setting the bulk field to zero (dashed lines) or inverting its sign (dotted lines). Ionizations due to the these electrons are therefore reduced. Energy gain by high-energy electrons is hindered by the true bulk field; altering the field configuration improves their ionization efficiency (see text). *The vertical scales for each initial electron energy are different.*

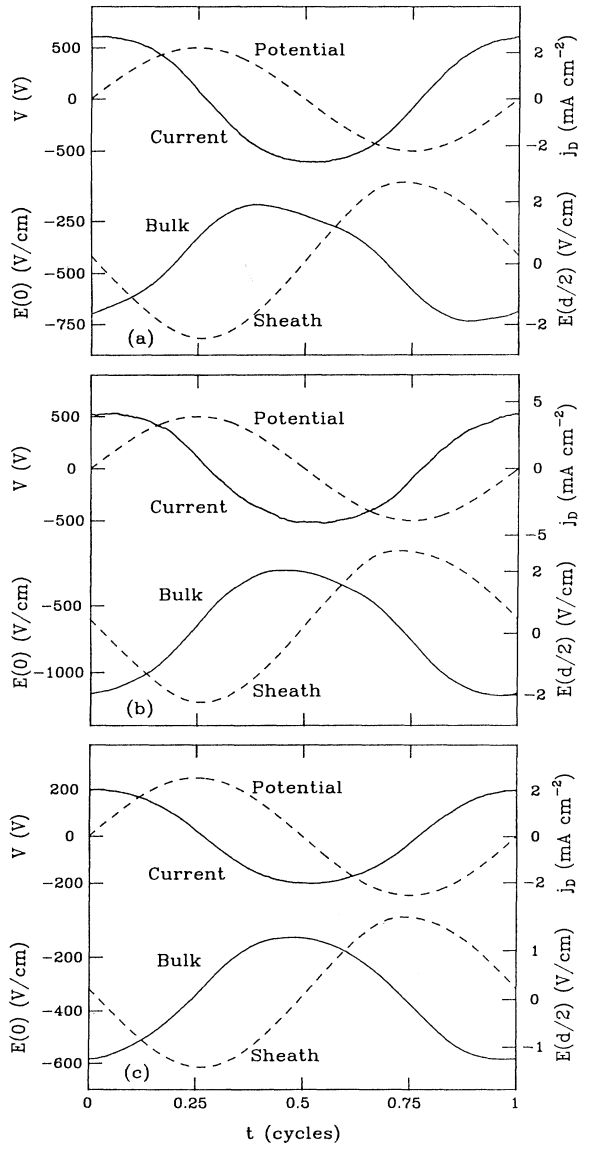

FIG. 4. The applied potential, discharge current, electric field at the $z=0$ cm electrode, and the bulk electric field (at $z=d/2$) for (a) the benchmark run, (b) run 7, and (c) run 10 over one rf cycle period.

Some conclusions can be drawn regarding the effects of E_{bulk}.

(1) Low-energy (≈ 0.5 eV) bulk electrons respond to E_{bulk}, but require on the order of an rf cycle ($T=7.375\times10^{-8}$ s) to cross the bulk and they undergo several collisions during the crossing. These low-energy electrons and the sheaths move at comparable speeds. Low-energy electrons are gently pushed by E_{bulk} toward an electrode as a sheath retreats toward that electrode. They move too slowly to catch the retreating sheath, bounce, and lose energy. These slow electrons are unable to move away before the subsequent sheath expansion, and are heated as the sheath moves past. Setting E_{bulk} to zero or inverting it inhibits the lowest-energy electrons from moving in behind the retreating sheath.

(2) Higher-energy electrons (≈ 15 eV) can cross the bulk several times per rf cycle and have twice the mean free path of the 0.5-eV electrons; they can cross the bulk and collide with a sheath at any time. They gain energy from the field during collisions with expanding sheaths and lose energy to the field upon hitting a contracting sheath [Fig. 3(c)], and the amount of energy gain or loss is dependent upon the relative speed of the electron and sheath. E_{bulk} hinders heating of these high-energy electrons because for most of an rf cycle it slows energetic electrons as they move through the bulk toward expanding sheaths (reducing the possible energy gain upon bouncing) and accelerates them as they move toward con-

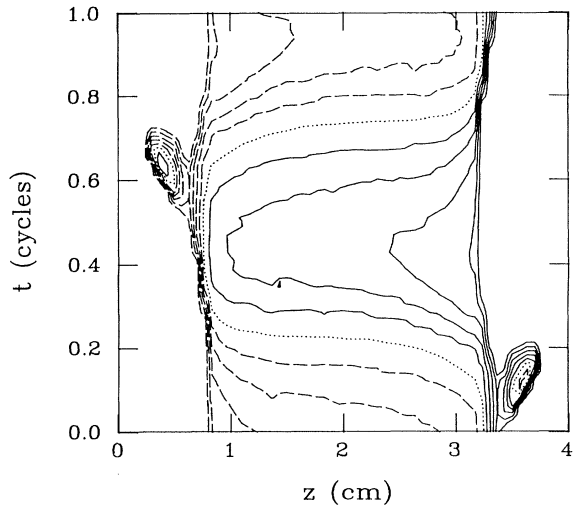

FIG. 6. The electric field for run 10 [see Fig. 3(a)]. The triple-field reversals appear as "islands" and arise from high-energy electrons which have been launched from the expanding sheath and have traversed the bulk plasma. The plot has been truncated at $E=\pm 3$ V/cm, and the contour spacing is 0.5 V/cm.

tracting sheaths (where their energy loss is magnified).

At higher neutral-particle densities we observe the formation of a triple-field reversal at the base of contracting sheaths which results in a second potential energy well for negatively charged particles (in addition to the potential minimum just discussed). Figure 6 is a contour plot of E for run 10. Hints of a similar structure exist in other runs, but only in run 10 do they result in a triple-field reversal. The appearance of the triple-field reversal coincides with the arrival of a beamlike group of high-energy electrons which originate in the expanding sheath (near the more distant electrode) and traverse the bulk plasma. These high-energy electrons do not appear to be secondaries; the triple-field reversal persists when run 10 is continued after setting $\gamma=0$. We therefore conclude that the high-energy electrons have been heated by sheath expansion and attribute their appearance in run 10 (and no other runs) to the additional avalanching which occurs at higher neutral densities. Verheest has shown that double layers can form in plasmas with only one positive-ion species if a two-temperature electron distribution exists.[105]

D. Electrode ion distribution and secondary electrons

As previously mentioned, the applied rf frequency is above the ion plasma frequency, and the ion density profile is therefore nearly independent of time. The ion velocity, however, does respond to the time-varying fields and its response is reflected in an $\approx 30\%$ variation in the ion current to each electrode during the rf cycle in the benchmark discharge.

We concentrate here on the ion distribution at the electrodes for the benchmark discharge conditions. Helium is not a useful etching gas, but the results provide some insight into the behavior of other noble-gas discharges, particularly argon, which is used for sputter etching, and some guidance for understanding the chemical-etching mechanism of reactive gases. The ion distribution at the electrodes is also measurable and provides contact between the present calculations and experiment.[66,67]

The solid lines in Fig. 7 show the ion distribution at the left ($z=0$) electrode in the benchmark discharge. A pulse of high-energy ions hits the electrode and peaks in energy $\approx\frac{1}{4}$ cycle after the maximum in the potential of the respective sheath. The high-energy tail of ions hitting the electrode persists to later times in the rf cycle. Hebner and Verdeyen[77] have seen the effects of such a time delay using a framing camera to track optical-line emission. Secondary electrons produced much of the observed emission in their experiment. The observed line intensity peaked well after the maximum sheath extent, indicating that the ion current to the electrode substantially lagged the maximum sheath extent.

The dashed lines in Fig. 7 show the distribution for a discharge at twice the neutral-particle density of the benchmark conditions. As expected, ions undergo more collisions as the gas density is increased, and their directed motion to the electrode is degraded. Lower applied discharge potentials have a similar effect on the directed ion motion. [It should also be noted that the ion distribution shown in Fig. 7 is plotted against only the ion velocity parallel to the discharge axis. It must be convoluted with a Maxwellian distribution of velocities transverse to the axis at the background gas temperature (300 K) to obtain the complete ion distribution function.]

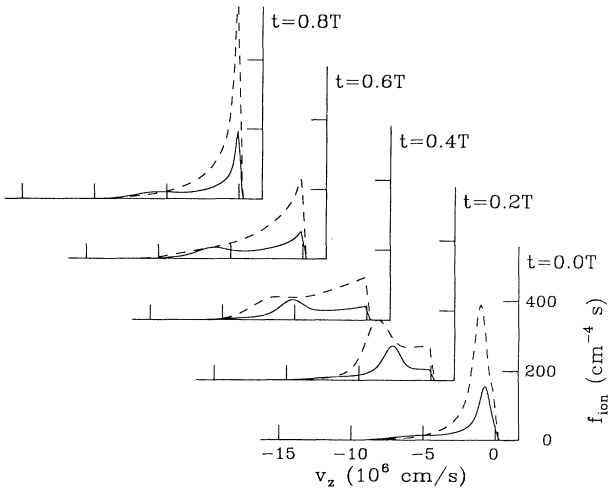

FIG. 7. The ion distribution f_i one-half cell from the left ($z=0$) electrode at five phases of the rf cycle. $f_i=N^{zv_z}/(A\Delta z\Delta v_z)$, where N^{zv_z} is the number of ions in the mesh cell centered at z and v_z and A is the discharge area. The solid line denotes benchmark discharge conditions; the dashed line indicates twice the neutral density but otherwise identical conditions (run 7).

The ion distribution function (IDF) at the electrodes has been measured and modeled for various discharge conditions.[60,87,106–109] Detailed structure in the IDF has been observed[106,109] in Ar discharges at low neutral-particle pressures (tens of mTorr). The structure arises because Ar^+ is more massive than He^+ and therefore remains in the sheath for more rf cycles. At lower neutral-particle densities fewer charge-exchange collisions occur and thus the ions are more likely to retain a memory of the oscillating sheath field. The simplified model of Wild and Koidl[106] is not appropriate for the conditions studied here. The more sophisticated model of Liu, Huppert, and Sawin[109] indicates that the structure vanishes even for the more massive Ar^+ at higher gas density.

Secondary electrons released from the electrodes by energetic ion impact play only a small role in maintaining these discharges; runs 3, 1, and 5 are only moderately different in spite of significant changes to the secondary-emission coefficient γ. Here γ is a coefficient for electron emission due only to ion bombardment of the electrodes. We have neglected electron emission due to metastable-atom bombardment. More He^+ than He^* is produced under the conditions studied here. All ions will eventually reach the walls while some of the metastable atoms will be collisionally quenched. Neglect of electron emission due to metastable-atom impact should not be serious because even the more plentiful secondary electrons produced by ion impact are relatively unimportant for these discharge conditions.

"Tracking" runs (described above) were used to study the fate of the secondary electrons. Only half of the secondary electrons launched during an rf cycle are still confined at the end of the cycle in the benchmark discharge. Those that remain have in general undergone one or more inelastic collisions, are less energetic, and are better confined; $>80\%$ of those remaining after the first rf cycle are still confined after two cycles. Changes to γ do not result in dramatic changes in discharge character, apparently because the long mean free path for ionization ($>d$ in the benchmark) prevents secondary electrons from avalanching extensively and allows many of the most energetic electrons to escape to an electrode before colliding. Secondary electrons are certainly not required to maintain the present discharges; $\gamma=0$ in runs 3 and 8.

E. Electron distribution function

Figures 8 and 9 are contour plots of the logarithm of the electron distribution function in the benchmark discharge at two instants in the rf cycle, $t=0$ and $t=T/4$, respectively (here, T indicates one rf cycle period). The upper plot of each figure shows the logarithm of the isotropic part of the distribution function ($\log_{10}[(\sum_\mu 2\pi v^2 \Delta\mu f_e)$ $\mathrm{cm^4\,s^{-1}}]$, where $f_e = N^{zv\mu}/(A\,\Delta z\,\Delta v\,\Delta\mu)$) plotted for all z and v. $N^{zv\mu}$ is the number of electrons in one mesh cell centered at z, v, and $\mu=\cos\theta$, and A is the discharge area. The volume of a mesh cell is $A\,\Delta z$ in real space and $\approx 2\pi v^2 \Delta v\,\Delta\mu$ in velocity space. The lower contour plot shows the logarithm of the full velocity distribution at the center ($z=d/2$) of the discharge ($\log_{10}[(2\pi v^2 f_e)\mathrm{cm^4\,s^{-1}}]$). Both figures are absolute. Zero (negative) contours correspond to regions where the plotted distribution is equal to (less than) unity, and the units of $2\pi v^2 f_e$ are $\mathrm{cm^{-4}\,s}$. Electrons at $\theta=0$ are moving in the $+z$ direction (from left to right in the plots), while electrons at $\theta=\pi/2$ are moving transversely, with a velocity parallel to the electrode faces. Two dominant features of all of the plots are the overwhelming number of low-energy bulk electrons and the contribution of the secondary electrons. We find that the inclusion of electron-electron scattering (see below) yields a more Maxwellian distribution than the results shown here (which do not include such Coulomb interactions).

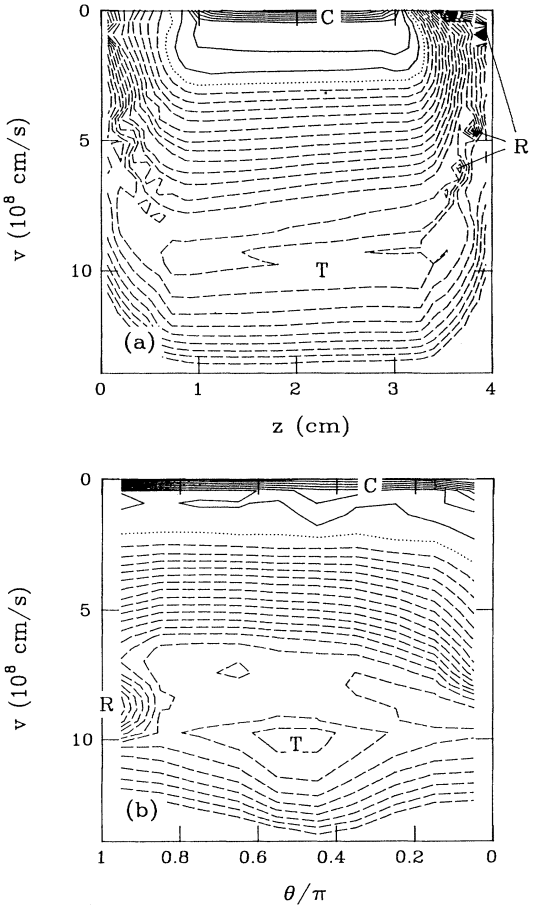

FIG. 8. Contour plots of $\log_{10}$ of portions of the electron distribution functions at time $t=0$ (see Fig. 3). The contour spacing is 0.25 (see text). (a) The logarithm of the isotropic part of the distribution function across the benchmark discharge. L and R label secondaries from the left ($z=0$ cm) and right ($z=4$ cm) electrode, respectively. T denotes a group of electrons moving transverse to the discharge axis. C labels the large number of low-energy (cold) bulk electrons. (b) The logarithm of the full angular and speed distribution at $z=d/2$.

As discussed above, the ion current to the each electrode significantly lags the instant of maximum sheath strength in the 0.1-Torr benchmark discharge. This is reflected in the distribution function of Fig. 8, at an in-

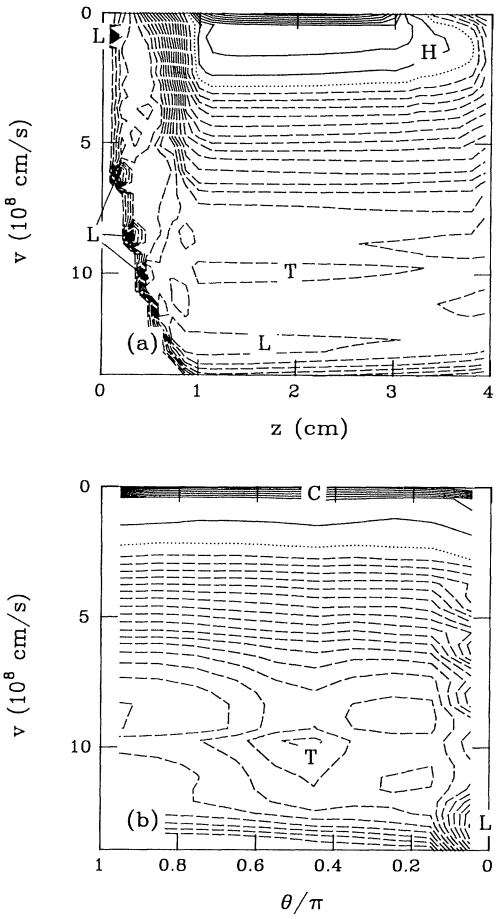

FIG. 9. Same as in Fig. 8, but at time $t=0.25T$ in the rf cycle of the benchmark discharge. *H* labels a relatively large density of low-energy electrons that has moved into a sheath region during what is periodically the anodic part of the rf cycle.

stant in the rf cycle where approximately equal potentials are dropped across each sheath, but when the $z=4$ cm sheath is collapsing from its maximum extent and the $z=0$ sheath is expanding. The ion current to the $z=0$ electrode has not had a chance to respond to the strengthening field, while ions hitting the $z=4$ cm electrode retain a memory of strong fields at an earlier phase of the rf cycle. A strong maximum in Fig. 8(b) at $\theta=\pi$ (labeled *R*) confirms the presence of secondary electrons from the $z=4$ cm electrode streaming through the bulk. These delayed secondaries are similar to those seen experimentally by Hebner and Verdeyen.[77]

The plots in Fig. 9 show the same information later in the rf cycle, at $t=T/4$, when the sheath near the $z=0$ electrode is maximum and the $z=4$ cm sheath is minimum. Secondary electrons from the $z=0$ electrode now dominate, as can be seen in Fig. 9(b). Figure 3 of Ref. 2 is an orthogonal projection of the information in Fig. 9(a).

A curious feature of both Figs. 8 and 9 is a group of relatively high-energy ($\approx$260 eV) electrons moving transverse to the discharge axis. Tracking calculations similar to those used to examine the role of the cold bulk electrons showed this local maximum to be composed of secondary electrons that have been scattered into the transverse direction. No such group of electrons appears in an otherwise identical discharge with $\gamma=0$ (run 3) or $V^0=250$ V (run 4), but does remain (at the same $\approx$260 eV energy) when the applied potential is doubled (run 6). The feature may be an artifact of replacing the full differential elastic cross section with the momentum transfer cross section.

High-energy electrons (say, $mv^2/2>|e|V^0/2$) are poorly confined because they are energetically able to escape to at least one electrode at any point in the rf cycle. The effect is very apparent in the distribution of high-energy electrons in the $V^0=1000$ V calculation (run 6), which is depleted of electrons moving predominantly parallel to the discharge axis.

A final important feature of Fig. 9 is the migration of a substantial number of low-energy electrons from the bulk region toward the $z=4$ cm electrode while the sheath near that electrode is minimum in extent (labeled *H*). It is these electrons which will be heated later in the rf cycle when the $z=4$ cm sheath again expands and sweeps them into the bulk. The dynamics of E_{bulk}, detailed earlier, aid this migration.

F. Bulk electron energy

The bulk electron energy is sensitive to the mechanism that sustains the discharge. In the parameter range considered here, it decreases as one increases neutral-particle density (compare runs 1 and 7), secondary-electron emission (runs 3, 1, and 5), applied voltage (runs 4, 1, and 6), or rf frequency (runs 2 and 1). Increasing the applied rf voltage or frequency enhances electron heating by sheath expansion and makes the bulk plasma more like a beam-sustained discharge. The bulk also has more of a beam-like component as secondary emission is increased. Higher neutral-particle densities aid discharge maintenance, both by improving ion confinement (reducing ion mobility), and by allowing more avalanching of high-energy (either secondary or sheath-heated) electrons. The quoted bulk energies are averages including electrons of all energies at $z=d/2$; the bulk energy is therefore decreasing (at higher V^0, f_0, γ, and N) in spite of an increasing density of very-high-energy beamlike electrons.

Figure 10 shows the time average of the mean bulk electron energy for the discharge studied as a function of Nd (product of neutral density and electrode spacing). Overlined quantities in this paper are time averaged over one rf cycle. Also plotted is the experimentally measured radiation temperature from Hebner, Verdeyen, and Kushner.[78] A CS calculation for these exact experimental discharge conditions is not feasible with our existing computers; however, the trends of the runs shown point to a very low bulk electron energy, approaching the neutral-particle gas energy, for discharges with larger Nd. The equal bulk energies found in runs 4 and 9 may arise from the fact that the discharge is barely sustained given these sets of operating parameters.

The bulk electron energy will not drop altogether to

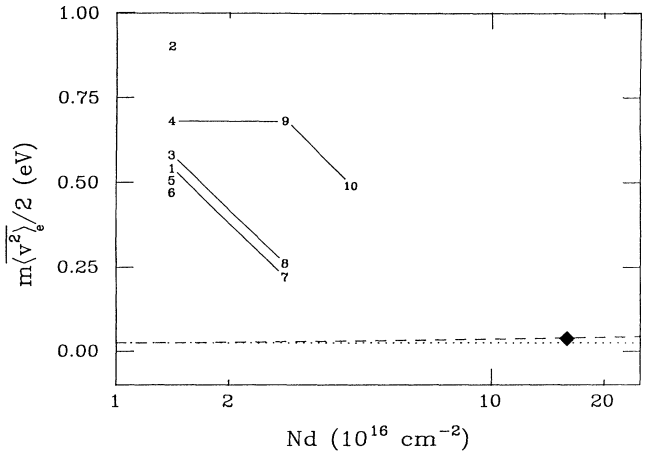

FIG. 10. Time-averaged mean electron energy at $z=d/2$ vs Nd. The plotted numbers correspond to the runs listed in Table II, and the experimental data point is from Ref. 78. The solid lines connect runs with identical V^0, f_0, and γ. The dotted line indicates the neutral-particle temperature (300 K) and the dashed line is very roughly the energy below which electron-stabilized recombination becomes important.

the gas temperature, even at very high Nd, because of Coulomb collisions transferring energy to very-low-energy electrons and other effects. The dashed line in Fig. 10 indicates very roughly where bulk plasma electron losses from electron-stabilized recombination[110] and ambipolar like diffusion losses are equal. The line shown assumes a peak plasma density of 10^{11} cm^{-3} and a bulk width of 2 cm. The recombination rate is strongly dependent on the electron energy; the dashed line (which indicates equal losses from diffusion and recombination) is therefore never far above the assumed neutral-particle temperature (dotted line). Longitudinal diffusion losses become less important as the length of the bulk region increases. Recombination provides a lower limit on the electron energy, both because electron losses increase dramatically as the electron energy approaches the gas temperature, and because recombination preferentially removes the very coldest bulk electrons.

We might also speculate that some discharges in electronegative gases may not contain the cold bulk electrons which are seen in these calculations and in various experiments. Discharge current in the bulk is resistive (in phase with the driving voltage) and carried by the electrons. The presence of negative ions in the bulk of an electronegative gas discharge may severely reduce the bulk electron density and therefore demand a higher electron velocity to carry the required current. A continuum model[20] has predicted an electron temperature of 5 eV in the bulk of an argonlike electronegative gas.

G. Higher-order processes

We have briefly investigated the effects of three higher-order processes in these rf discharges: multistep ionization due to metastable-atom–metastable-atom collisions, Coulomb collisions between electrons, and electron-ion recombination.

The time-averaged production rates per unit volume of singlet and triplet He metastable atoms and predicted metastable densities are shown in Fig. 11 for the benchmark discharge. The flat production profile in the bulk of the benchmark discharge is expected since the mean free path for excitation is many discharge lengths and since excitations are driven by the high-energy electrons that originate in the sheaths and cross the bulk. Production is more localized near the sheath-bulk boundary at higher N. In the lower-N cases the density profile of the triplet helium metastable atoms is dominantly that of a lowest-order diffusion mode, but the singlet-state-atom density profile is suppressed. At higher N the localized production near the sheath-bulk boundary and the shorter metastable-atom diffusion lengths yield a flat triplet-state-atom density profile. Singlet-state atoms are quenched by collisions with cold electrons [Eq. (8)]. This quenching is experimentally observable and has been used to estimate the density and temperature of the electrons in the negative glow of dc He discharges.[51]

It is beyond the scope of this paper to explore the effects of metastable-atom–metastable-atom (multistep) ionization over a wide range of parameter space. We have begun to investigate the effects of metastable-atom–metastable-atom collisions by coupling the multistep ionization rate back into the CS charged-particle calculation. For the benchmark conditions the increased total ionization rate results in a moderately higher peak plasma density (1.7×10^{10} cm^{-3}) and slightly lower bulk electron energy (0.50 eV). Figure 12 shows the results of coupling the multistep ionization due to metastable-atom–metastable-atom collisions back into the CS plasma calculation.

Multistep ionization should not be thought of as merely enhancing the electron-impact ionization rate by some

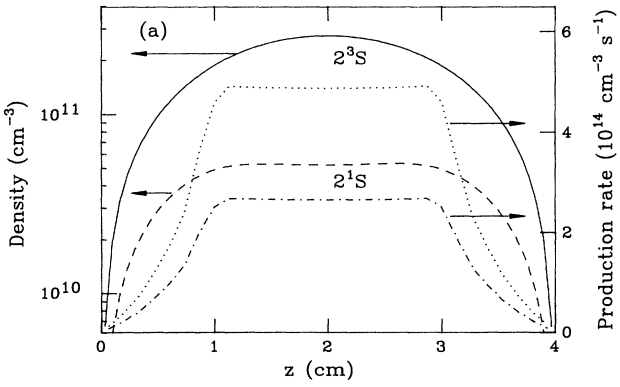

FIG. 11. Time-averaged metastable-atom production rate per unit volume and density in the benchmark discharge (no multistep ionization or e-e collisions). Note the suppression of the singlet-state atoms due to conversion of singlet- to triplet-state atoms in collisions with the numerous low-energy bulk electrons [Eq. (8)]. The production rates shown include cascade from higher levels.

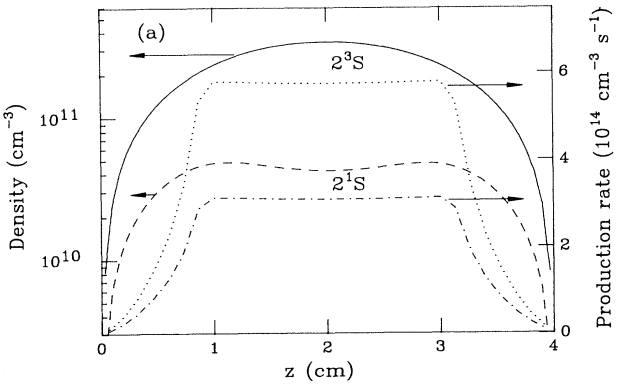

FIG. 12. Time-averaged metastable-atom production rate per unit volume and density in the benchmark discharge. The multistep ionizations due to metastable-atom–metastable-atom collisions are included, as are *e-e* collisions. Compare with Fig. 11.

fraction, but rather as a qualitatively distinct source of charged particles. Metastable-atom transport is not affected by the electric field; metastable atoms may freely diffuse into the sheaths, resulting in a large fractional increase of the charged-particle production near the electrodes. Metastable-atom–metastable-atom ionization in He always results in a rather energetic (≈ 15 eV) electron that can quickly reach the ionization threshold if produced in a high-field region. This electron is also more likely to reach an electrode because it can be produced near an electrode with significant kinetic energy and with an isotropic angular distribution. The sheath fields adjust themselves somewhat to offset the losses of these electrons. Such electrons could also be lost radially, so it might be expected that inclusion of radial losses would alter the trend observed here when multistep ionization is considered in the kinetic calculation.

Electron-electron (*e-e*) collisions might be important at these high plasma densities, and the results shown in Fig. 12 do include this effect. For the benchmark conditions shown in Table II, *e-e* collisions do not significantly alter most macroscopic quantities such as the plasma density, but do result in a slightly more Maxwellianlike distribution of electron velocities. More dramatic effects are observed when the plasma density is higher and the electron energy lower, as the *e-e* collision rate is proportional to $(n_e^2/\langle v\rangle_e^4)$.[91] Godyak and Piejak[69] have concluded that *e-e* collisions are important in an Ar discharge with a plasma density of 1.45×10^{10} cm^{-3} and a mean electron energy of 0.89 eV. For a given density and energy, *e-e* collisions may be more important in Ar than in He because of the Ramsauer minimum in the Ar collision cross sections.[69]

Electron-ion recombination has been included in all runs presented in this paper using rate coefficients from Deloche *et al.*[110] Recombination was not found to be important for any of the discharge conditions studied here.

H. Comparison to regional approximations

As mentioned in the literature review, discharge models built on traditional approximations are appealing because they require minimal computational effort. With results in hand from the CS method, which employs a minimum of approximations, we examine the validity of several typical regional descriptions in the hope of highlighting reliable approximations and possible improvements for such models.

Given the short mean free path for ion–neutral-particle charge exchange and that the rf frequency is larger than the ion plasma frequency, a regional model of the sheaths in the present discharges might assume collision-dominated, time-independent ion motion.[15] The ion velocity would then be obtained from the steady-state ion mobility and the local time-averaged electric field.

The present results indicate that the ion density is indeed nearly time independent, but that the ion velocity is not (see Fig. 7). At the instant of the rf cycle where the two sheaths are most similar, the ion velocity at each wall typically differs by a factor of 2. The ions in the expanding sheath have a memory of a lower field strength, and conversely in the contracting sheath (see Fig. 7).

The development of the "scale-up" method for speeding convergence (Appendix B) forced a detailed look at the correct averages required to accurately model the ion behavior; we found the time average of the mean ion velocity $\overline{\langle v_z\rangle_i}$ to be a crucial parameter for use in scale-up (where we want agreement at the percent level). The time average of the ion flux and of the mean ion velocity are directly proportional given the quasistationary ion density.

Many regional ion models obtain $\overline{\langle v_z\rangle_i}$ from the dc ion mobility μ_+ and the time-averaged field $\overline{E}$. This expression would reproduce $\overline{\langle v_z\rangle_i}$ exactly if μ_+ were field independent and if there were no inertial effects to retard attainment of the steady-state velocity. However, $\mu_+ \propto E^{-1/2}$ as E becomes large.[90,111,112] In spite of this discrepancy, and in spite of the temporal variations of $\langle v_z\rangle_i$, the dc mobility is in factor-of-2 agreement with the $\overline{\langle v_z\rangle_i}$ found from the CS (Fig. 13). The quality of agreement is not consistent throughout the discharge conditions studied here and is possible only given the actual $\overline{E}$ from the CS calculation. The largest discrepancies are found near the sheath-bulk boundary ($z\approx1.1$ cm and $z\approx2.9$ cm in Fig. 13).

Ambipolar diffusion is also a popular assumption for the bulk plasma region.[10,16,51] The ion velocity under the assumption of ambipolar diffusion is calculated from

$$\overline{\langle v_z\rangle_i}=\left[1+\frac{\overline{T}_e}{\overline{T}_i}\right]\frac{k\overline{T}_i\mu_+(\overline{E})}{|e|\overline{n}_i}\frac{d\overline{n}_i}{dz}\ , \tag{9}$$

where overlined quantities are the actual time-averaged results from the CS calculation and $\overline{T}_e$ and $\overline{T}_i$ are the time-averaged electron and ion temperatures, respectively. We have found the electron temperature T_e in terms of the mean random electron kinetic energy. The time-averaged electron temperature $\overline{T}_e$ is plotted in Fig. 13(a) and is used to plot $(k\overline{T}_e/M)^{1/2}$ in the left half of Fig. 13(b). Since the electron temperature is rather difficult to find from a regional model, a constant temperature is usually assumed.[16] A constant $\overline{T}_e$ is therefore plotted in the right half of Fig. 13(a) and used in the right half of

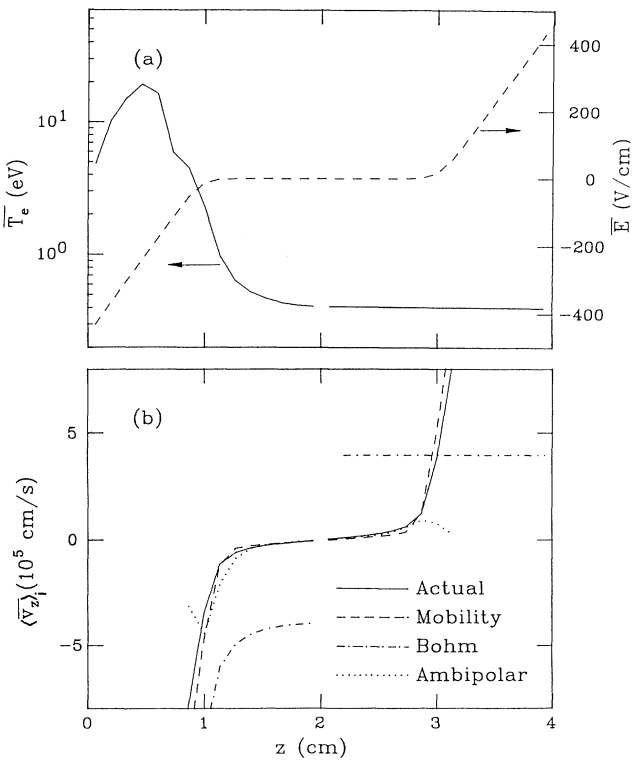

FIG. 13. Comparison of actual CS quantities and various regional approximations for the benchmark discharge. (a) The actual time-averaged electric field and electron temperature are plotted in the left half. The right half (a) shows the same field but a constant $\overline{T}_e$ set equal to the actual $\overline{T}_e(z=d/2)$. (b) The actual ion velocity is compared with $(k\overline{T}_e/M)^{1/2}$ (which is the Bohm velocity at the sheath edge), with the velocity obtained from the dc mobility and $\overline{E}$, and with the velocity consistent with ambipolar diffusion found using $\overline{T}_e$ (a).

Fig. 13(b), set equal to the value from the CS calculation at $z=d/2$ for the benchmark conditions. The $(k\overline{T}_e/M)^{1/2}$ in the right half of Fig. 13(b) reflects this constant $\overline{T}_e$.

The velocity found from the ambipolar model is quite accurate throughout the bulk. Surprisingly, the ambipolar velocity is closer near the sheath-bulk boundary under the assumption of a constant temperature $\overline{T}_e(d/2)$ in Fig. 13(b). The agreement is fortuitous; similar comparisons for the other runs indicate that the velocity found from Eq. (9) is generally reliable only to factors of 2 or 3.

The Bohm velocity is commonly used to join the sheath and bulk regions. The quantity $(k\overline{T}_e/M)^{1/2}$ is plotted as the dot-dashed line of Figs. 13(b); at the sheath edge this is the Bohm velocity. Defining the sheath edge is problematic. In this paper we have taken the location of the sheath-bulk boundary to be the location closest to the electrode where $\overline{E}<1$ V/cm; the electron and ion densities at this location are the same to better than 1%. The corresponding locations in the benchmark discharge (Fig. 13) are $z\approx 1.1$ cm $z\approx 2.9$ cm. Factor-of-2 agreement is perhaps the best that can be expected in joining the bulk and sheath regions, especially given the difficulty in defining the exact location of the boundary and the rapid spatial variation of particle density, velocity, and energy.

Regional calculations yield generally satisfactory results as long as the assumptions inherent in the particular approximation are valid. Given the $\overline{E}$ from the CS, the velocity found from the ion mobility is in reasonable (factor-of-2) agreement with the kinetic calculation over most of the discharge; the difficulty lies in finding the actual $\overline{E}$ in lieu of a self-consistent kinetic calculation. Because the dc electron mobility is a poor approximation at 13.56 MHz, one cannot accurately obtain the bulk field amplitude by setting the electron current amplitude at the discharge midplane $(z=d/2)$ equal to the discharge current and then using the dc electron mobility.

An ambipolar diffusion model is reasonable for ions in the bulk plasma, and ions in a collisional sheath can be described with a dc mobility. Joining such divergent approximations together is the apparent weakness in forming a regional model of the entire discharge. It is not obvious how to define the location of the bulk-sheath boundary. Approximations which work well in either the bulk or sheath are not reliable near the boundary region. The Bohm velocity, a commonly used workhorse for joining the bulk and plasma regions, contains the inherent assumptions of collisionless ions, inertialess electrons, and zero net current. It is not a satisfactory approximation in the discharges of interest here.

VII. SUMMARY

A numerical method based on propagators (Green's functions) has been used to model rf discharges, finding particle distributions consistently with the fields present, which are calculated from Poisson's equation. This convective scheme (CS) is an efficient algorithm applicable to a wide range of transport problems. Self-consistent kinetic calculations provide the most reliable predictions of discharge behavior because the required number of *ad-hoc* assumptions is minimized. Predictions of discharge behavior require only basic input data such as reactor geometry, collision cross sections and reaction rates, and applied voltage.

Quantitative comparison to experimental data is possible provided that the assumptions listed in Sec. IV are met, particularly the requirement that the experiment closely approximate an infinite-plane-parallel geometry. Helium was chosen as a discharge gas because important cross sections are known to good accuracy and because its chemistry is minimal. Use of a more complex molecular gas and inclusion of arbitrary chemical processes is straightfoward in principle, but the long time scale of such processes, coupled with the necessity of temporally resolving electron plasma oscillations, makes such calculations extremely long.

Electron and ion distributions were presented and display a rich variety of interesting dynamics. Ions do not respond instantly to the rf fields at low neutral-particle densities: in these discharges the flux of high-energy ions at the electrodes peaks $\approx T/4$ later than the instant of maximum sheath extent. The fluxes of secondary electrons released from the electrodes by ion impact reflect this time lag.

Helium metastable-atom densities were presented to facilitate contact with experimental measurements. Multistep ionization due to metastable-atom–metastable-atom collisions was found to decrease the average bulk electron energy and increase the bulk plasma density. The rapid conversion of singlet-state metastable atoms to triplet-state atoms during collisions with the cold bulk electrons produces a marked suppression of the singlet population, an easily observable feature which is strongly linked to the temperature and density of the bulk electrons.

Various common "regional" approximations were examined. Taken individually, many of the assumptions are in reasonable agreement with the self-consistent kinetic CS calculations. Difficulty arises both in using a sequence of assumptions and in joining the divergent assumptions made for the bulk and sheath regions into a model of the entire discharge.

A scale-up technique has been employed in an effort to reach convergence on the ion, rather than electron, time scale, and has made possible calculations at higher neutral densities. Implementation of scale-up demanded a clear understanding of which time-averaged electron quantities were fundamental to the ion calculation. We found the time-averaged mean ion velocity and ionization rate to be appropriate quantities for use in the ion calculation. Scale-up promises to expand the range of possibilities for future work: discharges at higher neutral-particle densities, with more interesting chemistry, and in electronegative gases.

Calculations using several sets of discharge parameters were presented to observe trends in discharge behavior. Consistent throughout the calculations was a low-average electron energy in the bulk regions and a weak bulk electric field substantially out of phase with the sheath fields. The bulk electron energy predicted by these self-consistent kinetic calculations is much lower than that of previous continuum[17] and Monte Carlo[52,53] calculations, but is in better general agreement with reliable experimental techniques.[78]

We have discussed experiments[10] and models[10,62] that identified two regimes of discharge operation. These works indicated that either bulk ionization (the α mechanism) or avalanching secondary electrons (the γ mechanism) can maintain the discharge.

We have argued in this work that secondary electrons play only a minimal role and that the discharge is not in the γ regime. Instead, power is deposited into the electrons primarily through temporal and spatial variations in the rf sheaths. Like the γ mechanism, heating due to sheath expansion produces a small number of energetic electrons which stream through the bulk region, drive excitation and ionization processes, and thus sustain the discharge. The bulk electrons may therefore have a very-low-average energy and need not directly participate in maintaining the discharge. Hebner *et al.*[77,78] concluded that the high-energy electrons inferred from their experiment were secondary electrons; no matter the source of the fast electrons, the beam-sustained bulk plasma is a common feature of both the present calculations and their experiment.

A correct description of the bulk power balance, as can be provided by the CS, is required to confidently move on to an accurate model of plasma chemistry, especially negative-ion formation. Attachment cross sections are very sensitive to the electron energy; reliable estimates of this process and other plasma chemistry rates require a precise knowledge of the bulk electron dynamics.

APPENDIX A: ENERGY-CONSERVING CS

This Appendix presents details of the improvements made to the CS subsequent to the description given in Ref. 1. The discussion centers on the conservation of energy on a numerical mesh with cells spaced at constant increments in velocity. Following the nomenclature of Ref. 1, the *initial* cell is a mesh cell where particles exist prior to a time step, the *moved* cell is the location and size of the region found by moving the *initial* cell along the appropriate phase-space trajectory defined by the initial coordinates and the fields present. The *final* cells are the mesh cells overlapped by the *moved* cell. In general, the *moved* cell does not correspond to a single cell in the mesh. Doubly and singly primed indices denote the quantities before and after a time step, respectively.

One deficiency of the original method can be immediately seen in Fig. 2: There is no zero-energy cell on the mesh. A zero-velocity mesh cell was previously excluded so as to avoid problems with singularities in the equations of motion at $v_z=0$. In the original implementation, particles which are stopped after a time step (either by a collision which has left them with zero energy or because they were initially moving against the field and have now stopped) cannot be placed in the mesh with zero kinetic energy. Rather, they are split equally between the cells straddling the $v_z=0$ axis, properly leaving them with no net velocity but improperly adding $m(\Delta v_z/2)^2/2$ to the kinetic energy of each particle. The obvious solution is to modify the mesh so that a cell centered on $v_z=0$ exists. Singularities are less of a problem than first thought.

The second source of error is less obvious and is associated with the discrete nature of the allowed velocities on the mesh. Consider the mesh of Fig. 2 and a cell containing n particles which, after a time step, has velocity $(Q'+q'-\frac{1}{2})\Delta v_z$, where q' is an integer which indexes the cell velocity Q' is a real number $0\le Q'<1$, and Δv_z is the width of the cell in the velocity coordinate (see the upper half of Fig. 2). For the moment we ignore the need to place particles in appropriate spatial bins and we take the size of the *moved* cell Δv_z to be the same as the mesh cells. The particles in the *moved* cell must now be split in some fashion between cells centered at $(q'-\frac{1}{2})\Delta v_z$ and $(q'+\frac{1}{2})\Delta v_z$. The simplest version of the method dictates placing $(1-Q')n$ of the particles in a *final* cell with index

q' centered at $(q'-\frac{1}{2})\Delta v_z$ and $Q'n$ of the particles in a *final* cell with index $q'+1$ centered at $(q'+\frac{1}{2})\Delta v_z$.

Now we check for energy conservation. The velocity associated with the *moved* cell is $(q'-\frac{1}{2}+Q')\Delta v_z$, so the kinetic energy of its n particles is $n\frac{1}{2}m[(q'-\frac{1}{2}+Q')\Delta v_z]^2$. After being split between the two *final* mesh cells, their kinetic energy is

$$n(1-Q')\tfrac{1}{2}m[(q'-\tfrac{1}{2})\Delta v_z]^2+nQ'\tfrac{1}{2}m[(q'+\tfrac{1}{2})\Delta v_z]^2 ;$$

the kinetic energy has increased by $n\frac{1}{2}mQ'(1-Q')(\Delta v_z)^2$ in the process of distributing particles back into the mesh. The error is always non-negative; thus the process of distributing particles back into the mesh uniformly increases their kinetic energy.

We emphasize that the errors in the energy are not associated with the equations of motion or the velocity of the *moved* cell, but rather with the process of distributing particles back into a mesh which allows only discrete velocities. The simple CS would conserve energy if the mesh was uniformly spaced in energy, rather than velocity, but a velocity mesh was chosen so as to improve energy resolution for low-energy particles. The dc cathode-fall results of Ref. 1 were not unduly hindered by imperfect energy conservation because no field reversals were allowed to form and hence no trapped particles existed. The total error in the energy is directly related to the number of times the particles are moved and redistributed, and in Ref. 1 electrons did not dwell in the discharge long enough for the errors in their energy to become a significant fraction of their true energy. Trapped electrons exist in the rf discharges of interest here, however, and energy conservation must be strictly enforced.

The energy conserving algorithm is therefore the following.

(1) For each cell of the mesh, utilizing the initial position and velocity and the fields present, find the position and velocity of the *moved* cell. This process is exactly as before.[1] As presently implemented, each face of the *initial* cell [at $(p''-1)\Delta z$ and $p''\Delta z$, where p'' is an integer which indexes the *initial* cell position] is independently moved to a trial final position, then the mean of the fields at the initial position and the trial final position are used to find the actual position of each face of the *moved* cell. The averaging process can be repeated if necessary, or replaced with a more sophisticated particle mover.

(2) From the spatial extent of the *moved* cell, determine the number of particles in the *moved* cell which will be placed in the cells with each spatial index, also as before. For the example in Fig. 2, $(1-P')n$ particles will be placed in cells with spatial index p' and $P'n$ particles in cells with spatial index $p'+1$.

(3) For each possible *final* spatial index, find the pair of cells with adjacent velocity indices whose total energy (kinetic plus potential) straddles the total energy of the *moved* cell and split the particles between these pairs of cells so as the preserve the energy of the *moved* cell. If φ denotes the electric potential in a cell, we obtain the final velocity v_z' by requiring conservation of total energy for each final spatial index (the description here being for electrons):

$$\tfrac{1}{2}m(v_z')^2-e\varphi'=\tfrac{1}{2}m(v_z'')^2-e\varphi'' . \tag{A1}$$

(4) Q' is then found from v_z' such that $v_z'=(q'-\frac{1}{2}+Q')\Delta v_z$, q' is an integer, and $0\le Q'<1$. We now find a fraction F

$$F=\frac{Q'(Q'+2q'-1)}{2q'} \tag{A2}$$

which is in general different for each spatial index because the Q' was found by enforcing conservation of total energy independently for each final spatial index. Finally, the particles are distributed to each final cell so as to conserve energy thus

$$\begin{aligned}
&n(1-P')[1-F(p'-\tfrac{1}{2})] \text{ into cell } p',q' ,\\
&n(1-P')F(p'-\tfrac{1}{2}) \text{ into cell } p',q'+1 ,\\
&nP'[1-F(p'+\tfrac{1}{2})] \text{ into cell } p'+1,q' ,\\
&nP'F(p'+\tfrac{1}{2}) \text{ into cell } p'+1,q'+1 .
\end{aligned} \tag{A3}$$

An exception exists to the above prescription which is also necessary to conserve energy. If the particles are moving into a region of higher potential energy (against the force) it may be energetically impossible for them to reach all of the cells overlapped by the *moved* cell. The problem arises when particles move only a small fraction of a cell "up the potential hill" before being reflected by the field (they are energetically unable to reach the center of the next cell). The simple CS dictates that some particles be placed in a cell, but to do so would violate energy conservation. The solution is to place the particles that would have gone into an energetically forbidden cell into the last energetically allowed spatial cell traversed and then reverse their velocity, thus accounting for the reflection.

The discussion thus far has considered only a CS implemented with two independent variables, a spatial coordinate z and the velocity along that coordinate v_z. The changes required to extend the energy conserving algorithm to more independent variables (such as those used to describe electron motion in this paper) are straight forward.

Precise energy conservation may or may not be important for an accurate calculation. It affects only ballistic movement, and some collisions can erase the memory of any energy errors prior to the collision. This is the case for the helium ions; charge-exchange collisions are so frequent that energy errors are unable to accumulate before a collision occurs. What errors do exist manifest themselves only as a small error in the apparent ion mobility.

Energy conservation is important for electrons because electrons remain in the discharge long enough for these increases in electron energy to lead to excess ionization, which can drastically affect the accuracy of the calculation.

APPENDIX B: RAPID CONVERGENCE

As has been found by others,[17,22,64,113,114] convergence of rf discharge calculations is a nontrivial matter. The absolute number density, for instance, may grow by a small amount for many ($10-10^4$) cycles, with the problem worsening at higher neutral-particle densities as the ion confinement-time grows. Models (including the CS), which explicitly integrate forward in time until a steady state is reached, are ordinarily limited to a time step less than the electron plasma period ($\Delta t < 2\pi/\omega_{pe}$) to preserve numerical stability and accuracy, which is less than a nanosecond for the discharges of interest here.

A simple method of reducing run time was used in Ref. 2 and consisted of monitoring trends during a calculation (peak plasma density, for instance), stopping the run, increasing or decreasing the density, restarting, and again monitoring trends. Changing the density was handled as follows: The ion distribution function was uniformly multiplied by a scaling factor chosen to achieve the desired peak ion density. The electron distribution was then multiplicatively scaled at each spatial location so as to be consistent with the last-known instantaneous field configuration. (Instantaneous, here and in what follows, refers to an instant in the rf cycle.) A negative-electron density may be implied at some locations to achieve the original field; the electron density was simply set to zero in these locations. The robustness of the CS allows an easy start even from this inconsistent initial condition, though some degree of harshness does occur and with it some excess heating and ionization. The calculation then proceeds from this point until the inevitable transients vanish and longer-term trends can once again be established.

A more sophisticated method is used here, and represents an attempt to reach convergence on the ion-confinement time scale. The calculation is started by running both ions and electrons for some time in a full mode. (In this Appendix, "full" refers to the usual CS calculation of both electrons and ions, advanced on the electron plasma time scale, $\Delta t < 2\pi/\omega_{pe}$.) This calculation allows initial transients to relax. Starting with a distribution function even remotely similar to that expected during the actual calculation greatly speeds this initial phase of the calculation.

Three important quantities are tabulated during each rf cycle of the full calculation, the time averages of the ionization rate per unit volume $\bar{S}$, the ion density $\bar{n}_i$ and the average ion velocity $\overline{\langle v_z \rangle}_i$. (The ion density profile is very insensitive to the rapid rf field oscillations since $2\pi f_0 > \omega_{pi}$; hence the ion density n_i at any given phase of the rf cycle is approximately the time-averaged value $\bar{n}_i$.) These quantities are then used to guide a "scale-up" during which the CS calculations follows the ions alone for many scale-up cycles. The electric field for the scale-up cycles is chosen such that the time-averaged mean-ion-velocity profile $\overline{\langle v_z \rangle}_i$ is reproduced exactly at the start of a scale-up.

Utilizing the time-averaged ionization rate per unit volume $\bar{S}$ from the full run and the field just prescribed, the ion distribution is integrated forward in time using the CS. This constitutes the "scale-up."

The important result of the scale-up is a new ion density profile. The ion density profile from the scale-up is used to multiplicatively scale the last-known instantaneous ion velocity distribution (saved previously) at each spatial location; this yields an ion distribution which reflects both the density obtained from the scale-up and the instantaneous ion velocity information appropriate for that instant of the cycle. The electron distribution is adjusted, as in the simpler method, multiplicatively at each spatial point so that the electron density is consistent with the combination of the new ion density and the last-known instantaneous field.

We then return to the full calculation, advancing both electrons and ions with $\Delta t < 2\pi/\omega_{pe}$. It should be noted that integral numbers of full and scale-up cycles are run, with the switchover always occurring at the same phase of the rf cycle.

Given a fixed ionization rate per unit volume and average-ion-velocity profile, an analytical expression can also be found for a scale-up corresponding to any given length of time. The calculation for intermediate times is rather tedious, but since the CS code already exists, we use the just-described method to advance the ion density through a scale-up. The analytic expression for very long times (a scale-up of infinite length) is very simple, however. This infinite scale-up has not been extensively used for actually advancing the discharge calculation, but has been quite useful as another test of convergence.

The development of this scale-up procedure has made it evident that care must be taken to eliminate inconsistencies when switching between the full and scale-up portions of the calculation. This included an effort to find the best possible field for use during the scale-up, and the use of the previous instantaneous field and particle velocity information. Inconsistencies tend to manifest themselves as excess electron heating and thus as ionization upon returning to the full calculation, and in degraded convergence characteristics. As a final effort to eliminate inconsistencies, the ionization rate per unit volume over the last full cycle prior to a scale-up is saved for use in the first cycle after the scale-up. This allows transients to relax in the first cycle of the next full run without leading to excess ionization.

Under the discharge conditions examined in this paper, convergence can typically be reached in ≈ 5 scale-up iterations, each such iteration consisting of a full run of 3–5 rf cycles and an ion scale-up phase of 10^2-10^3 rf cycles. Slow electron processes such as energy loss due to elastic collisions of electrons with neutral particles might in principle not be adequately handled because the full electron calculation may only be run for tens of rf cycles, not thousands. (Examination of electron behavior tends to rule out such processes in these discharges because each electron is frequently heated by the oscillating sheaths.) The full calculation is therefore resumed after

completion of the ≈ 5 scale-up iterations. It is only from the results of this final full run (both ions and electrons, no scale-up, and with $\Delta t < 2\pi/\omega_{pe}$) that the calculation may finally be declared converged.

Many numerical methods that follow the time evolution of a discharge may benefit from a procedure similar to "scale-up." A more general discussion of methods for rapidly converging discharge calculations, along with a more detailed discussion of the scale-up technique employed here, will appear in a separate paper.[115]

---

*Present address: Department of Electrical and Computer Engineering, University of Illinois at Urbana-Champaign, Urbana, IL 61801.

[1]T. J. Sommerer, W. N. G. Hitchon, and J. E. Lawler, Phys. Rev. A **39**, 6356 (1989).
[2]T. J. Sommerer, W. N. G. Hitchon, and J. E. Lawler, Phys. Rev. Lett. **63**, 2361 (1989).
[3]W. N. G. Hitchon, D. J. Koch, and J. B. Adams, J. Comput. Phys. **83**, 79 (1989).
[4]P. Bletzinger and Mark J. Flemming, J. Appl. Phys. **62**, 4688 (1987).
[5]P. Bletzinger, J. Appl. Phys. **67**, 130 (1990).
[6]K. Köhler, J. W. Coburn, D. E. Horne, E. Kay, and J. H. Keller, J. Appl. Phys. **57**, 59 (1985).
[7]V. A. Godyak, Fiz. Plazmy **2**, 141 (1976) [Sov. J. Plasma Phys. **2**, 78 (1976)].
[8]V. A. Godyak and Z. Kh. Ganna, Fiz. Plazmy **6**, 676 (1980) [Sov. J. Plasma Phys. **6**, 372 (1980)].
[9]V. A. Godyak and A. Kh. Ganna, Fiz. Plazmy **5**, 670 (1979) [Sov. J. Plasma Phys. **5**, 376 (1979)].
[10]V. A. Godyak and A. S. Khanneh, IEEE Trans. Plasma Sci. **PS-14**, 112 (1986).
[11]Valery A. Godyak and Natalia Sternberg, Phys. Rev. A **42**, 2299 (1990).
[12]J. H. Keller and W. B. Pennebaker, IBM J. Res. Dev. **23**, 3 (1979).
[13]W. B. Pennebaker, IBM J. Res. Dev. **23**, 16 (1979).
[14]Michael A. Lieberman, IEEE Trans. Plasma Sci. **16**, 638 (1988).
[15]Michael A. Lieberman, IEEE Trans. Plasma Sci. **17**, 338 (1989).
[16]G. R. Misium, A. J. Lichtenberg, and M. A. Lieberman, J. Vac. Sci. Technol. A **7**, 1007 (1989).
[17]David B. Graves and Klavs F. Jensen, IEEE Trans. Plasma Sci. **PS-14**, 78 (1986).
[18]P. Bayle, J. Vacquie, and M. Bayle, Phys. Rev. A **34**, 360 (1986).
[19]Michael S. Barnes, Tina J. Colter, and Michael E. Elta, J. Appl. Phys. **61**, 81 (1987).
[20]Yong-Ho Oh, Nak-Heon Choi, and Duk-In Choi, J. Appl. Phys. **67**, 3264 (1990).
[21]J. P. Boeuf, J. Appl. Phys. **63**, 1342 (1988).
[22]J. P. Boeuf, Phys. Rev. A **36**, 2782 (1987).
[23]J. Dutton, J. Phys. Chem. Ref. Data **4**, 577 (1975).
[24]P. Segur, M. Yousfi, J. P. Boeuf, E. Marode, A. J. Davies, and J. G. Evans, in *Electrical Breakdown and Discharges in Gases,* Vol. 89A of *NATO Advanced Study Institute, Series B: Physics,* edited by E. E. Kunhardt and L. H. Luessen (Plenum, New York, 1983), p. 331.
[25]John H. Ingold, in *Gaseous Electronics,* edited by M. N. Hirsh and H. J. Oskam (Academic, New York, 1978), Vol. I, Chap. 2, p. 37.
[26]J. H. Ingold, Phys. Rev. A **40**, 3855 (1989).
[27]A. V. Phelps, B. M. Jelenković, and L. C. Pitchford, Phys. Rev. A **36**, 5327 (1987).
[28]K. Kitamori, H. Tagashira, and Y. Sakai, J. Phys. D **11**, 283 (1978).
[29]J. Lucas and H. T. Saelee, J. Phys. D **8**, 640 (1975).
[30]H. Tagashira, Y. Sakai, and S. Sakamoto, J. Phys. D **10**, 1051 (1977).
[31]Y. Sakai, H. Tagashira, and S. Sakamoto, J. Phys. D **10**, 1035 (1977).
[32]R. Courant, K. Friedrichs, and H. Lewy, Math. Ann. **100**, 32 (1928).
[33]Jay P. Boris and David L. Book, J. Comput. Phys. **11**, 38 (1973).
[34]D. L. Book, J. P. Boris, and K. Hain, J. Comput. Phys. **18**, 248 (1975).
[35]J. P. Boris and D. L. Book, J. Comput. Phys. **20**, 397 (1976).
[36]J. P. Boris and D. L. Book, Methods Comput. Phys. **16**, 85 (1976).
[37]Steven T. Zalesak, J. Comput. Phys. **31**, 335 (1979).
[38]John V. DiCarlo and Mark J. Kushner, J. Appl. Phys. **66**, 5763 (1989).
[39]Pierre Segur and Robert Keller, J. Comput. Phys. **24**, 43 (1977).
[40]J. P. Boeuf and E. Marode, J. Phys. D **15**, 2169 (1982).
[41]A. V. Phelps and L. C. Pitchford, Phys. Rev. A **31**, 2932 (1985).
[42]L. C. Pitchford, in *Electrical Breakdown and Discharges in Gases* (Ref. 24), p. 313.
[43]S. Yachi, Y. Kitamura, K. Kitamori, and H. Tagashira, J. Phys. D **21**, 914 (1988).
[44]H. Itoh, N. Ikuta, and K. Toyota, J. Phys. D **16**, 293 (1983).
[45]Tran Ngoc An, E. Marode, and P. C. Johnson, J. Phys. D **10**, 2317 (1977).
[46]R. J. Carman and A. Maitland, J. Phys. D **20**, 1021 (1987).
[47]R. J. Carman, J. Phys. D **22**, 55 (1989).
[48]M. Ohuchi, and T. Kubota, J. Phys. D **16**, 1705 (1983).
[49]Seishiro Hashiguchi and Mitugi Hasikuni, Jpn. J. Appl. Phys. **27**, 1010 (1988).
[50]T. J. Moratz, L. C. Pitchford, and J. N. Bardsley, J. Appl. Phys. **61**, 2146 (1987).
[51]E. A. Den Hartog, D. A. Doughty, and J. E. Lawler, Phys. Rev. A **38**, 2471 (1988).
[52]M. J. Kushner, J. Appl. Phys. **54**, 4958 (1983).
[53]Mark J. Kushner, IEEE Trans. Plasma Sci. **PS-14**, 188 (1986).
[54]R. W. Hockney and J. W. Eastwood, *Computer Simulation Using Particles* (McGraw-Hill, New York, 1981).
[55]Charles K. Birdsall and A. Bruce Langdon, *Plasma Physics via Computer Simulation* (McGraw-Hill, New York, 1985).
[56]R. W. Boswell and I. J. Morey, Appl. Phys. Lett. **52**, 21 (1988).
[57]M. Surendra, D. B. Graves, and I. J. Morey, Appl. Phys. Lett. **56**, 1022 (1990).
[58]D. B. Graves (private communication).
[59]A. Date, K. Kitamori, and H. Tagashira, in *Nonequilibrium*

Processes in Partially Ionized Gases, Vol. 220 of *NATO Advanced Study Institute Series B: Physics* edited by Mario Capitelli and J. Norman Bardsley (Plenum, New York, 1990), p. 433.
[60]David Vender and Rod W. Boswell, IEEE Trans. Plasma Sci. **PS-18**, 725 (1990).
[61]J. P. Boeuf and Ph. Belenguer, in *Nonequilibrium Processes in Partially Ionized Gases* (Ref. 59), p. 155.
[62]Ph. Belenguer and J. P. Boeuf, Phys. Rev. A **41**, 4447 (1990).
[63]H. Debontride, J. Derouard, P. Edel, R. Romestain, N. Sadeghi, and J. P. Boeuf, Phys. Rev. A **40**, 5208 (1989).
[64]M. Surendra, D. B. Graves, and G. M. Jellum, Phys. Rev. A **41**, 1112 (1990).
[65]Karl H. Schoenbach, Hao Chen, and G. Schaefer, J. Appl, Phys. **67**, 154 (1990).
[66]W. D. Davis and T. A. Vanderslice, Phys. Rev. **131**, 219 (1963).
[67]J. W. Coburn and Eric Kay, J. Appl. Phys. **43**, 4965 (1972).
[68]V. Godyak and R. Piejak (unpublished).
[69]Valery A. Godyak and R. B. Piejak, Phys. Rev. Lett. **65**, 996 (1990).
[70]V. A. Godyak and R. B Piejak, J. Vac. Sci. Technol. A **8**, 3833 (1990).
[71]V. A. Godyak and R. B Piejak, J. Appl. Phys. **68**, 3157 (1990).
[72]S. M. Levitskii, Zh. Tekh. Fiz. **27**, 970 (1957) [Sov. Phys. Tech. Phys. **2**, 887 (1957)].
[73]O. A. Popov and V. A. Godyak, J. Appl. Phys. **57**, 53 (1985).
[74]Cameron A. Moore, Glenn P. Davis, and Richard A. Gottscho, Phys. Rev. Lett. **52**, 538 (1984).
[75]Richard A. Gottscho and Carl E. Gaebe, IEEE Trans. Plasma Sci. **PS-14**, 92 (1986).
[76]Richard A. Gottscho, Phys. Rev. A **36**, 2233 (1987).
[77]G. A. Hebner and J. T. Verdeyen, IEEE Trans. Plasma. Sci. **PS-14**, 132 (1986).
[78]G. A. Hebner, J. T. Verdeyen, and M. J. Kushner, J. Appl. Phys. **63**, 2226 (1988).
[79]D. K. Doughty, S. Salih, and J. E. Lawler, Phys. Lett. **103A**, 41 (1984).
[80]D. K. Doughty and J. E. Lawler, Appl. Phys. Lett. **45**, 611 (1984).
[81]D. A. Doughty, E. A. Den Hartog, and J. E. Lawler, Phys. Rev. Lett. **58**, 2668 (1987).
[82]E. A. Den Hartog, T. R. O'Brian, and J. E. Lawler, Phys. Rev. Lett. **62**, 1500 (1989).
[83]John. M. Anderson, Phys. Rev. **108**, 898 (1957).
[84]J. M. Anderson, J. Appl. Phys. **31**, 511 (1960).
[85]Anonymous, Bull. Am. Phys. Soc. **34**, 295 (1989); P. J. Hargis, Jr., K. E. Greenberg, P. A. Miller, J. B. Gerardo, R. A. Gottscho, A. Garscadden, P. Bletzinger, J. R. Roberts, J. K. Olthoff, J. R. Whetstone, R. J. Van Brunt, H. M. Anderson, M. Splichal, J. L. Mock, M. L. Passow, M. L. Brake, M. E. Elta, D. B. Graves, M. J. Kushner, J. T. Verdeyan, G. Selwyn, M. Dalvie, J. W. Butterbaugh, H. H. Sawin, T. R. Turner, and R. Horwath, Bull. Am. Phys. Soc. **36**, 195 (1991).
[86]J. E. Lawler, Phys. Rev. A **32**, 2977 (1985).
[87]Brian E. Thompson, Herbert H. Sawin, and Donald A. Fisher, J. Appl. Phys. **63**, 2241 (1988).
[88]G. D. Alkhazov, Zh. Tekh. Fiz. **40**, 97 (1970) [Sov. Phys. Tech. Phys. **15**, 66 (1970)].
[89]R. W. LaBahn and J. Callaway, Phys. Rev. A **2**, 366 (1970), Phys. Rev. **180**, 91 (1969); **188**, 520 (1969).
[90]H. Helm, J. Phys. B **10**, 3683 (1977).
[91]Yilin Weng and Mark J. Kushner, Phys. Rev. A **42**, 6192 (1990).
[92]J. B. Adams and W. N. G. Hitchon, J. Comput. Phys. **76**, 159 (1988).
[93]J. B. Adams, W. N. G. Hitchon, and L. M. Holzmann, J. Vac. Sci. Technol. A **6**, 2029 (1988).
[94]W. N. G. Hitchon, D. J. Koch, and W. D. D'haeseleer, Nucl. Fusion **29**, 1675 (1989).
[95]D. J. Koch and W. N. G. Hitchon, Phys. Fluids B **1**, 2239 (1989).
[96]W. N. G. Hitchon, J. Plasma Phys. **41**, 323 (1989).
[97]A. W. Ali and H. R. Griem, Phys. Rev. **140**, A1044 (1965).
[98]C. van Trigt, Phys. Rev. **181**, 97 (1969).
[99]W. L. Wiese, M. W. Smith, and B. M. Glennon, *Atomic Transition Probabilities,* Natl. Bur. Stand. Ref. Data Ser., Natl. Bur. Stand. (U.S.) Circ. No. 4 (U.S. GPO, Washington, D.C., 1966), Vol. I.
[100]M. F. Wehner and W. G. Wolfer, Phys. Rev. A **27**, 2663 (1983).
[101]W. C. Fon, K. A. Berrington, P. G. Burke, and A. E. Kingston, J. Phys. B **14**, 2921 (1981).
[102]A. V. Phelps, Phys. Rev. **99**, 1307 (1955).
[103]A. V. Phelps and J. P. Molnar, Phys. Rev. **89**, 1202 (1953).
[104]A. H. Sato and M. A. Lieberman, J. Appl. Phys. **68**, 6117 (1990).
[105]Frank Verheest, J. Plasma Phys. **42**, 395 (1989).
[106]Ch. Wild and P. Koidl, Appl. Phys. Lett. **54**, 505 (1989).
[107]M. F. Toups and D. W. Ernie, J. Appl. Phys. **68**, 6125 (1990).
[108]S. G. Ingram and J. St. J. Braithwaite, J. Appl. Phys. **68**, 5519 (1990).
[109]J. Liu, G. L. Huppert, and H. H. Sawin, J. Appl. Phys. **68**, 3916 (1990).
[110]R. Deloche, P. Monchicourt, M. Cheret, and F. Lambert, Phys. Rev. A **13**, 1140 (1976).
[111]L. S. Frost, Phys. Rev. **105**, 354 (1957).
[112]Gregory H. Wannier, *Statistical Physics* (Wiley, New York, 1966), p. 464.
[113]J. P. Boeuf (private communication).
[114]M. Surendra (private communication).
[115]W. N. G. Hitchon, T. J. Sommerer, and J. E. Lawler, IEEE Trans. Plasma Sci. **PS-19** (to be published).